Applications of the method

Clément Ernould[a,b], **Benoît Beausir**[a,b,*], **Jean-Jacques Fundenberger**[a,b], **Vincent Taupin**[a,b], **and Emmanuel Bouzy**[a,b]
[a]Université de Lorraine, CNRS, LEM3, Metz, France
[b]Laboratory of Excellence on Design of Alloy Metals for low-mAss Structures (DAMAS), University of Lorraine, Metz, France
*Corresponding author: e-mail address: benoit.beausir@univ-lorraine.fr

Contents

Advances in Imaging and Electron Physics
ISSN 1076-5670
https://doi.org/10.1016/bs.aiep.2022.07.005

1. Introduction

1.1 Context

For reminder, the present work was conducted as part of the first author's PhD at the University of Lorraine from 2017 to 2020 (Ernould, 2020). It deals with the development of a high-angular resolution method for the measurement lattice rotations and elastic strains in the scanning electron microscope (Ernould, Beausir, Fundenberger, Taupin, & Bouzy, 2020a, 2020b, 2021). This kind of technique is known as the HR-EBSD or, more recently, the HR-TKD technique, depending on whether it is applied to electron backscatter diffraction (EBSD) patterns or transmission Kikuchi diffraction (TKD) patterns. In the following, "HR-EBSD/TKD" will be employed when no distinction is needed regarding the SEM-based configuration used.

The HR-EBSD/TKD technique determines the elastic deformation gradient tensor $\boldsymbol{F}^e$ between two points of the crystal from the displacement field between their respective diffraction patterns, knowing the projection geometry and assuming a traction free-surface surface. However, this is a very delicate task for which two main research efforts can be identified. The first one is the projection geometry, i.e., the position of the pattern center (PC) and the sample-to-detector distance (DD), as well as its variations across the orientation. These parameters need to be determined accurately, namely about 0.05% of the pattern width (Britton et al., 2010; Maurice, Dzieciol, & Fortunier, 2011). The second one is the measurement of the displacement field with subpixel accuracy using digital image registration techniques (Villert, Maurice, Wyon, & Fortunier, 2009, p. 200; Wilkinson, Meaden, & Dingley, 2006a, 2006b) (see Chapter "Measuring elastic strains and orientation gradients by scanning electron microscopy: Conventional and emerging methods" by Ernould et al. for more details).

The present work focuses on measuring the displacement field sought by HR-EBSD/TKD techniques. The latter can be perfectly described by a linear homography, i.e., a line but not edge preserving transformation often met in photogrammetry to model projections, as demonstrated in Chapter "Development of a homography-based global DIC approach for high-angular resolution in the SEM" by Ernould et al. Such a shape function implies eight parameters, from which the components of the deviatoric deformation gradient tensor $\widehat{\boldsymbol{F}}^e$ are analytically deduced knowing the projection geometry. Because the homography assumption is valid at the scale of the scintillator, a unique and large region of interest is considered by the digital image correlation (DIC) analysis. The proposed method is therefore a global DIC approach. It contrasts with the original "local" approach (Wilkinson et al., 2006a, 2006b), which relies on shift measurements between several small square subsets picked up across the patterns.

The implementation of the method is detailed in Chapter "Implementing the homography-based global HR-EBSD/TKD approach" by Ernould et al. Patterns are first pre-aligned by means of Fourier-Mellin and Fourier-transform based cross-correlation algorithms to estimate their relative in-plane rotation and translation, respectively. These measurements provide an initial guess of the homography at the beginning of the subsequent inverse-compositional Gauss-Newton (IC-GN) algorithm. It is an iterative optimization algorithm in the spatial domain used for subpixel registration. It is modified by integrating a correction of optical distortions caused by camera lenses. The whole method is validated numerically in Chapter "Numerical validation and influence of optical distortions on accuracy" by Ernould et al., which also tackles the necessity of such a correction.

1.2 Content of the chapter

This chapter proposes five applications of the method: three plastically deformed metals and two semiconductors. For the former, aim is to characterize deformation structures in terms of grain internal disorientation angle and geometrically necessary dislocation (GND) densities. For the latter, focus is on measuring elastic strains. In both cases, the EBSD and the on-axis TKD techniques are used.

In a first step, the SEM used is presented. Definitions of the grain internal disorientation angle and of the GND densities are given. Pattern filtering is detailed and illustrated.

In a second step, applications to plastically deformed metals are proposed. Dislocations structures in an interstitial free (IF) steel subjected to 15% tensile deformation are characterized by means of HR-EBSD. The contribution of the global cross-correlation based initial guess on performances is quantified. Two on-axis HR-TKD analyses are also carried out in quenched and tempered martensitic steel as well as in nanocrystalline aluminum obtained by severe plastic deformation. The microscope used is pushed to the maximum of its possibilities in the latter example.

In a third step, elastic strains in semi-conductors are investigated. On-axis HR-TKD measurements in the vicinity of $Si_{1-x}Ge_x$ epitaxial layer are compared to nano-beam electron diffraction (NBED) in the transmission electron microscope (TEM). Regarding the HR-EBSD technique, GaN single crystal containing threading dislocations bounding domains disorientated by about 0.1° is considered.

Finally, results are discussed and summarized before concluding this series of five chapters.

2. SEM and data analysis

2.1 Scanning electron microscope and cameras

The experimental datasets studied in this chapter are acquired using a Zeiss Supra 40 SEM equipped with a Schottky field emission gun (Fig. 1). This technology offers a probe size close to the nanometer, compared to 3 to 5 nm for thermionic emission guns (Brisset, Repoux, Ruste, Grillon, & Robaut, 2008). This is essential for the characterization of nanocrystalline materials by means of on-axis TKD. Moreover, electron beam brightness, i.e., the current density per unit solid angle, is of the order of 10^7 A.cm^{-2}.sr^{-1} (compared to 10^5). This lowers exposure times and thus beam drift considerations, which is of particular interest for on-axis TKD analyses. The latter are indeed performed at a magnification of ×36,000 to ×500,000 in the following.

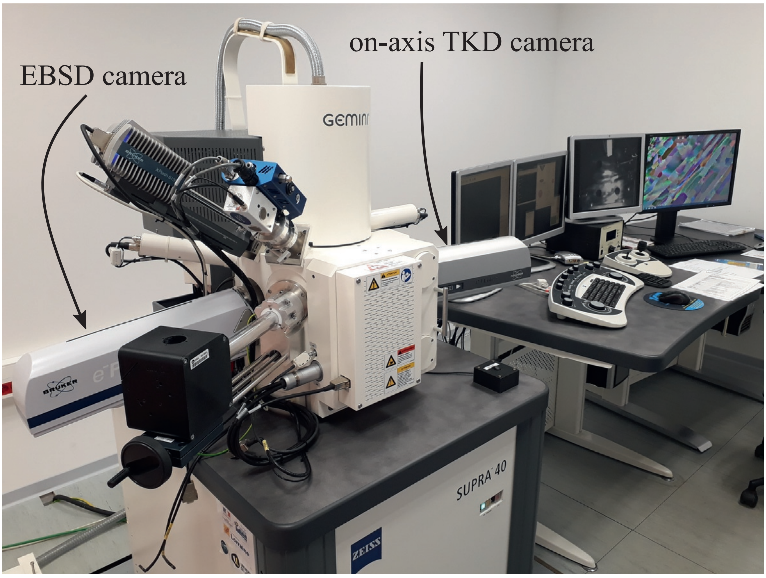

Fig. 1 Zeiss Supra 40 FEG-SEM used in this study.

The microscope is equipped with two Bruker e-Flash HR+ cameras: one for EBSD and the other associated with the Bruker Optimus™ detector head for on-axis TKD. These cameras have a charge-coupled device (CCD) photographic sensor with maximum resolutions of 1600×1200 or 1200×1200 pixels and 8- or 16-bit grayscale. A Bruker Argus™ sensor is attached to each camera. It detects backscattered electrons (EBSD) or forward-scattered electrons (TKD on-axis), but will be referred to as FSD detector (forescatter electron diodes) thereafter. As detailed in Chapter "Measuring elastic strains and orientation gradients by scanning electron microscopy: Conventional and emerging methods" by Ernould et al., FSD contrast is highly sensitive to crystal orientation, topography, as well as phases. It provides qualitative information about the sample surface (EBSD) or the entire thin foil thickness (on-axis TKD). Therefore, FSD images will help to assess the relevance of HR-EBSD/TKD measurements.

2.2 Factors limiting accuracy

Diffraction patterns are indexed by the Bruker ESPRIT 1.9 commercial software. It uses the Hough-transform, whose resolution is set to maximum. Calibration principle is based on the iterative fitting technique (Krieger Lassen, 1999). Its accuracy is about 0.5% of the pattern width. Although this is insufficient for accurate elastic strain measurement (Britton et al., 2010; Villert et al., 2009), it is considered anyway when deducing the deviatoric deformation gradient tensor $\widehat{\boldsymbol{F}}^{e}$ from the measured homography. Consequently, phantom strains of the order of 10^{-3} are to be expected (see section 3.4.3 in Chapter "Measuring elastic strains and orientation gradients by scanning electron microscopy: Conventional and emerging methods" by Ernould et al. for more details). Probe displacement is accounting for, knowing the sample and camera tilt angles of EBSD scans. It is neglected regarding on-axis TKD, the largest map being barely three microns wide.

Optical distortions of our cameras are unknown and the correction is disabled during the IC-GN algorithm. However, neglecting optical distortions is assumed reasonable in the proposed examples, i.e., those distortions are expected to introduce relative errors of <10% based on Chapter "Numerical validation and influence of optical distortions on accuracy" by Ernould et al. Indeed, applications in the plastically deformed metals focuses on lattice rotations in the presence of disorientations up to about 10 degrees. Regarding the on-axis TKD application to $Si_{1-x}Ge_x$, elastic strains are expected to be about 2% while no notable rotation is present.

Finally, both small rotations and elastic strains ($\leq 2 \times 10^{-3}$) will be measured from an EBSD dataset in GaN single crystal, courtesy of Dr. Haithem Mansour. It is acquired using another SEM equipped with an optical distortion-free Oxford Symmetry camera. The projection geometry is determined in Aztec software by coupling the moving screen technique with pattern matching.

2.3 Disorientation angle and GND densities

The grain internal disorientation angle $\Delta\theta$ between the reference ("A") and each of the other pixels in the grain ("B") is calculated from their respective orientation matrices $\boldsymbol{g_A}$ and $\boldsymbol{g_B}$, which are derived from the Euler angles obtained by Hough-transform based indexing (HTI). The disorientation angle is

$$\Delta\theta = \min_k \left[\arccos\left(\frac{\mathrm{tr}(\boldsymbol{\Delta g}^k) - 1}{2} \right) \right], \tag{1}$$

where

$$\boldsymbol{\Delta g^k} = \left(\boldsymbol{s}^k.\boldsymbol{g_B}\right).\left(\boldsymbol{s}^k.\boldsymbol{g_A}\right)^{-1} \tag{2}$$

is the "disorientation" matrix for the k-th symmetry of the crystal. This disorientation is decomposed into three rotations w_i^{HTI} with respect to the axes $\vec{X}_i$ of the sample frame:

$$w_i^{HTI} = -e_{ijk}.\Delta g_{ij}.\frac{\Delta\theta}{2.\sin(\Delta\theta)}, \tag{3}$$

where e_{ijk} is the permutation symbol of Levi-Civita. Note that,

$$w_{ij} = -e_{ijk} w_k, \tag{4}$$

which means:

$$\begin{cases} w_1 = w_{32} = -w_{23} \\ w_2 = w_{13} = -w_{31} \\ w_3 = w_{21} = -w_{12} \end{cases}. \tag{5}$$

The homography is initialized from these rotations in case of an indexing-based initial guess (see section 4.1 in Chapter "Implementing the homography-based global HR-EBSD/TKD approach" by Ernould et al.).

According to the Nye-Kröner theory (Kröner, 1958; Nye, 1953), the Nye's dislocation density tensor is

$$\boldsymbol{\alpha} = \boldsymbol{curl}\,\boldsymbol{\varepsilon} + tr(\boldsymbol{\kappa_e}).\boldsymbol{I} - \boldsymbol{\kappa_e}^T, \tag{6}$$

where $\boldsymbol{\varepsilon}$ is the elastic strain tensor and $\boldsymbol{\kappa_e}$ the lattice curvatures. The latter are approximated with a finite difference scheme:

$$\kappa_{ij} \cong \Delta w_i / \Delta x_j, \tag{7}$$

where Δw_i is the difference of rotation w_i between two neighboring points separated spatially by Δx_j in the j-th direction. The Nye tensor is computation as follows

$$\boldsymbol{\alpha} = \begin{bmatrix} \frac{\partial \varepsilon_{12}}{\partial x_3} - \frac{\partial \varepsilon_{13}}{\partial x_2} & \frac{\partial \varepsilon_{13}}{\partial x_1} - \frac{\partial \varepsilon_{11}}{\partial x_3} & \frac{\partial \varepsilon_{11}}{\partial x_2} - \frac{\partial \varepsilon_{12}}{\partial x_1} \\ \frac{\partial \varepsilon_{22}}{\partial x_3} - \frac{\partial \varepsilon_{23}}{\partial x_2} & \frac{\partial \varepsilon_{23}}{\partial x_1} - \frac{\partial \varepsilon_{21}}{\partial x_3} & \frac{\partial \varepsilon_{21}}{\partial x_2} - \frac{\partial \varepsilon_{22}}{\partial x_1} \\ \frac{\partial \varepsilon_{32}}{\partial x_3} - \frac{\partial \varepsilon_{33}}{\partial x_2} & \frac{\partial \varepsilon_{33}}{\partial x_1} - \frac{\partial \varepsilon_{31}}{\partial x_3} & \frac{\partial \varepsilon_{31}}{\partial x_2} - \frac{\partial \varepsilon_{32}}{\partial x_1} \end{bmatrix} + \begin{bmatrix} \frac{\partial w_{12}}{\partial x_3} + \frac{\partial w_{31}}{\partial x_2} & \frac{\partial w_{13}}{\partial x_1} & \frac{\partial w_{21}}{\partial x_1} \\ \frac{\partial w_{32}}{\partial x_2} & \frac{\partial w_{23}}{\partial x_1} + \frac{\partial w_{12}}{\partial x_3} & \frac{\partial w_{21}}{\partial x_2} \\ \frac{\partial w_{32}}{\partial x_3} & \frac{\partial w_{13}}{\partial x_3} & \frac{\partial w_{31}}{\partial x_2} + \frac{\partial w_{23}}{\partial x_1} \end{bmatrix}, \tag{8}$$

and its entrywise norm is:

$$\|\boldsymbol{\alpha}\| = \sqrt{\alpha_{ij}.\alpha_{ij}}. \tag{9}$$

Due to the two-dimensional nature of orientation mappings, it is not possible to compute the entire Nye tensor. Spatial derivatives along the surface normal direction ($\overrightarrow{X_3}$) in Eq. (8) are unknown. Only α_{13}, α_{23} and α_{33} components are fully assessable (El-Dasher, Adams, & Rollett, 2003; Pantleon, 2008; Sun, Adams, & King, 2000). The α_{12} and α_{21} components are determined by neglecting the contribution of elastic strains, which is partly unknown. Finally, the components α_{31} and α_{32} are not computable, neither the contribution of lattice curvatures nor that of elastic strains being fully assessable. Finally, the α_{ij} components have units of inverse length. In this chapter, they are expressed in μm^{-1}, or in m^{-2} by dividing them by the norm b of the Burgers vector.

2.4 Data analysis and pattern filtering

Acquisition parameters will be detailed for each application, but in all cases, 16-bits diffraction patterns are recorded. Apart from the application in GaN, patterns are saved without any background correction in a *.bcf file by the Bruker ESPRIT 1.9 software, which is then imported into ATEX-software, developed at our lab (Beausir & Fundenberger, 2017). It is also responsible for the automatic selection of the reference patterns.

As detailed in Chapter "Implementing the homography-based global HR-EBSD/TKD approach" by Ernould et al., the software also provides a user graphical interface and send instructions to the Fortran program conducting the DIC analysis. Unless otherwise stated, patterns are pre-aligned by the proposed global cross-correlation-based initial guess, from which the homography is fully initialized. Regarding the IC-GN algorithm, a convergence criterion C_{conv} of 0.001 pixel and a maximum number of iterations n_{max} of 200 are set.

At the end of the analysis, the Fortran program returns a file containing, among others, the elastic strain components ε_{ij} and the crystal rotations w_{ij} in the sample frame. The left polar decomposition of the deformation gradient tensor is considered for their computation. Then, grain internal disorientation and GND densities are calculated and displayed in ATEX-software.

During the DIC analysis, patterns are filtered according to the four following steps:

1) The continuous background due to inelastic scattering is removed. Unless a background image is available, a logarithmic high-pass spatial filter is applied:

$$\hat{s}(x, y) = N^2.\log[\mathrm{s}(x, y) + 1] - \sum_{i=-\mathrm{n}}^{n} \sum_{j=-n}^{n} \log[s(x+i, y+j) + 1] \qquad (10)$$

where $s(x, y)$ et $\widehat{s}(x, y)$ are the initial and filtered intensities and $N = 2n + 1$ is the kernel size.

2) A Gaussian filter with a radius of 1 or 2 pixels is applied to reduce noise and improves the convergence speed of the IC-GN algorithm without loss of accuracy (see section 3.3.2 in Chapter "Numerical validation and influence of optical distortions on accuracy" by Ernould et al.).

3) Intensities are zero-mean and normalized, i.e., their average is 0 and their standard deviation is 1. Extremes values are truncated at ± 3.5.

4) If necessary, a mask containing noise is applied to the reference pattern in order to hide dust on the scintillator or the transmitted beam and diffraction spots in the central region of on-axis TKD patterns.

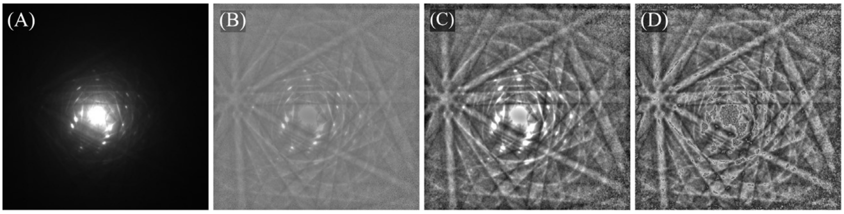

Fig. 2 Filtering steps of an on-axis TKD pattern. (A) Raw pattern. (B) After removing the continuous background using a logarithmic high-pass filter. (C) After normalizing intensities. (D) After applying a mask with noise on diffraction spots and one the transmitted beam.

Fig. 2 illustrates these steps from an on-axis TKD pattern of size a 600×600-pixels. As compared to EBSD and conventional TKD, on-axis TKD patterns show a much larger dynamics in intensities (Fig. 2A). After applying a logarithmic high-pass filter of size $N = 71$ pixels, intensity is relatively uniform across the whole pattern (Fig. 2B). A Gaussian filter of radius one pixel is applied, and the intensities are zero-mean normalized (Fig. 2C). If it is the reference pattern, a mask containing noise is applied to diffraction spots and the transmitted beam (Fig. 2D). To do so, pixels having an intensity twice higher than the standard deviation are considered in descending order. Given a pixel, it is added to the mask which propagates to neighboring pixels and so on as long as intensities are decreasing.

3. Deformation structures in plastically deformed metals

Plastically deformed metals are characterized in terms of grain internal disorientation angle and GND densities. A thin foil of tempered 9Cr-ODS (oxide dispersed strengthened) martensitic steel is first observed using on-axis TKD. Then, a sample of IF steel deformed by 15% in uniaxial tension testing is characterized by EBSD. It shows disorientations up to 12°, allowing to experimentally evaluate the contribution of the global cross-correlation (GCC) based initial guess on the numerical efficiency of the IC-GN algorithm. Note that they are some differences with already published results (Ernould et al., 2020a). More specifically, the number of iterations was reduced thanks to some code improvements as mentioned in the discussion of Chapter "Implementing the homography-based global HR-EBSD/TKD approach" by Ernould et al.

3.1 On-axis HR-TKD analysis in quenched and tempered 9Cr-ODS steel

3.1.1 Material and acquisition parameters

9Cr-ODS martensitic steel is austenitized at 1050 °C for 10 min, quenched with helium gas, and tempered at 600 °C for 20 min before air cooling. Strong plastic shear deformations are generated during martensitic transformation. Then, partial recovery of strains and dislocation substructures occurs during the tempering treatment. A thin foil is obtained by twinjet electro polishing is characterized by means of on-axis TKD.

Acquisition parameters are summed up in Table 1. The thin foil is mapped at a magnification of ×37,000 with a step size of 10 nm. To ensure the best possible lateral spatial resolution, a low probe current of 1.25 nA is used (low current mode) while the accelerating voltage is maximal (30 kV). At this scale, beam drift is a major problem. Diffraction patterns with medium resolution of 600 × 600 pixels are consequently acquired with an exposure time of 40 ms without frame averaging. Anyway, the sharpness of the diffraction contrast is mostly degraded by plastic deformation and

Table 1 Acquisition parameters of the on-axis TKD dataset in ODS steel.

On-axis TKD configuration	
Working distance (*WD*)	3.75 mm
Sample-to-detector distance (*DD*)	24.63 mm
Sample tilt	0°
Detector tilt	0.4° (with respect to the horizontal)
Orientation map	
Magnification	×37,000
Step size	10 nm
Map size	3.09 × 2.32 μm^2 (71,688 points)
Pattern acquisition	
Accelerating voltage	30 kV
Probe current	1.25 nA (central aperture: 60 μm)
Pattern resolution	600 × 600 pixels (pixel size: 40 μm)
Exposure time	40 ms
Frame averaging	1

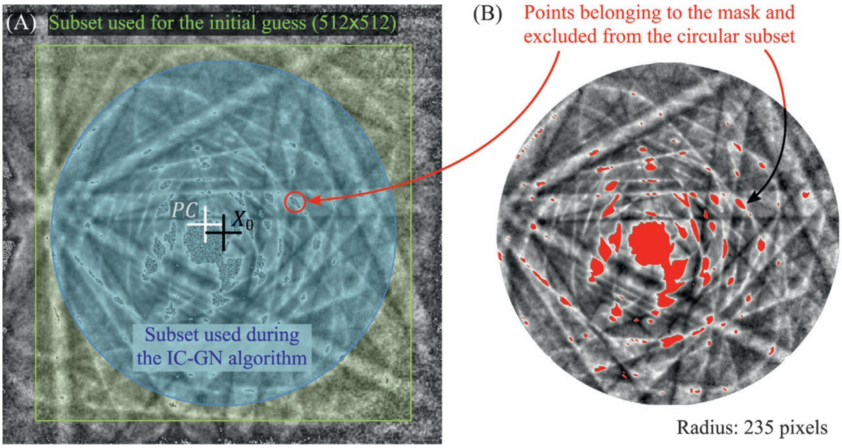

Fig. 3 (A) Position, size and shape of the regions of interest used for the DIC analysis of on-axis TKD patterns acquired in ODS steel. (B) Exclusion of points belonging to the mask from the subset used for subpixel registration. The pattern displayed is the reference of the large central grain of the map (marked with a white cross in Fig. 4A).

cannot be significantly improved by longer exposure times. Note that the pattern displayed in Figs. 2 and 3 is the reference of the large grain in the center of the map in Fig. 4A, where the reference patterns are spotted by white crosses. Its signal-to-noise ratio is one of the highest among all the dataset.

A square subset of size 512 × 512 pixels (green region in Fig. 3A) and a circular subset of radius 235 pixels (blue) are considered by the GCC-based initial guess and the IC-GN algorithm, respectively. However, points belonging to the mask (highlighted in red in Fig. 3B) are excluded from the second subset. Since the mask is specific to each reference pattern, the number of points within the subset slightly varies from one grain to another.

3.1.2 Grain internal disorientation and GND mappings

Fig. 4 compares on-axis HR-TKD results with those obtained from HTI. The noise on the grain internal disorientation angle derived from crystallographic orientations is about 0.5° (Fig. 4A and red profile in Fig. 5A). The uncertainty in the disorientation axis strongly reduces the sensitivity of the GND calculation (Fig. 4B). Only subgrain boundaries with disorientation greater than ~2.5° stand out from the background, as shown by the three peaks in the red profile in Fig. 5B.

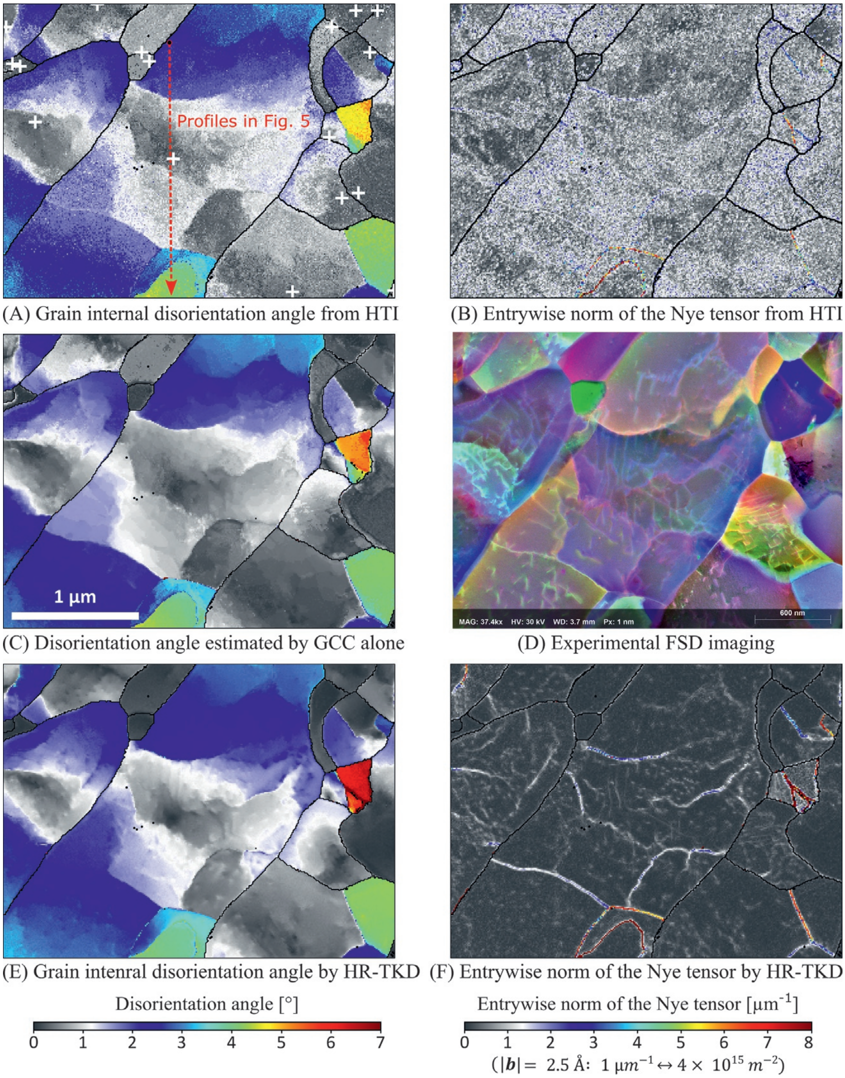

Fig. 4 On-axis TKD map in ODS steel. (A) Grain internal disorientation angle derived from HTI. White crosses indicate the reference patterns. (B) Associated norm of the Nye tensor. Similarly, (E) and (F) correspond to the results of the HR-TKD analysis. (C) Grain internal disorientation angle estimated by the GCC-based initial guess alone. (D) Experimental FSD image.

Alone, the GCC-based initial guess already yields to a noise reduction on the disorientation angle (Fig. 4C). This is particularly visible at low disorientations (<1,5°), consistently with the error of less than 0.25° determined during the numerical validation (section 3.2.1 in Chapter "Numerical

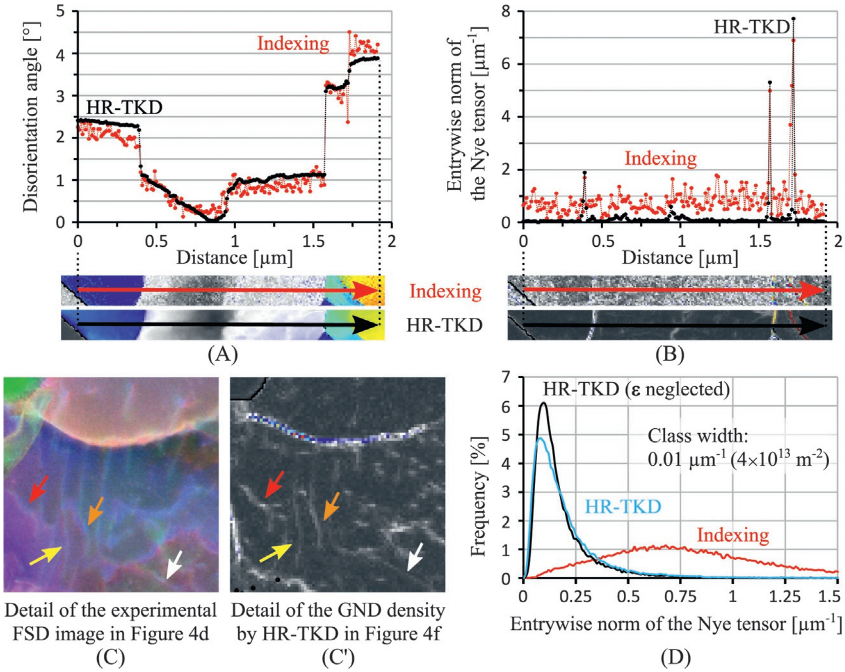

Fig. 5 Profiles of (A) the grain internal disorientation angle and of (B) the entrywise norm of the Nye tensor determined by HR-TKD (black) or from indexing (red). The location of the profile is drawn in red in Fig. 4A. (C) Detail of the FSD image in Fig. 4D compared to (C′) the GND density by HR-TKD in Fig. 4D. (D) Distribution of the entrywise norm of the Nye tensor for different approaches.

validation and influence of optical distortions on accuracy" by Ernould et al.). Moreover, the initial guess ensures a convergence of the IC-GN algorithm at almost any point of the map. The presence of sudden orientation changes is not a hindrance as the initialization strategy is path-independent (see section 4.1.1 in Chapter "Implementing the homography-based global HR-EBSD/TKD approach" by Ernould et al.).

The indexing software is not dedicated to on-axis TKD patterns. The Hough transform tends to identify Kikuchi band edges rather than their centers due to the asymmetry of band contrast in transmission (Niessen, Burrows and Fanta, 2018). This can lead to systematic error on the disorientation angle between two subgrains, hence the relatively constant gap between disorientation profiles in Fig. 5A. Therefore, a comparison between the GCC-based and the indexing-based initial guess strategies will be performed later considering EBSD patterns.

The true solution being unknown, the FSD image (Fig. 4C) allows the relevance of the maps obtained by on-axis HR-TKD (Fig. 4E,F) to be qualitatively assessed. Indeed, FSD contrast essentially shows an orientation contrast, the foil thickness being assumed constant over the observed region (~7 μm^2) and a single phase being present (aside from chromium nano-precipitates, which appear as pink or purple spots).

Despite the medium resolution and quality of the patterns as compared to HR-EBSD standards, the proposed method succeeds in highlighting fine details of the deformed microstructure. Isolated dislocations in the FSD image (Fig. 5C) are also visible in the GND density map (Fig. 5C'). Note that the FSD image provides information on the entire thickness of the foil, whereas electrons contributing to Kikuchi diffraction patterns stem from the bottom face of the sample. Therefore, some details of the FSD image may not be catch by on-axis HR-TKD.

Due to insufficient accuracy on calibration and possible presence of optical distortions, elastic strains are uncertain. They are shown as an indication in Fig. 6, but they are neglected in the calculation of the entrywise norm of the Nye tensor in Fig. 4F. Taking them into account does not significantly change the latter. It is slightly noisier, as suggested by the lower peak height of the distribution in Fig. 5D, where the blue curve (considering $\boldsymbol{\varepsilon}$) is to be compared to the black one ($\boldsymbol{\varepsilon}$ neglected). Apart from their magnitude, the elastic strain mappings (Fig. 6) appear to be generally plausible, with some details qualitatively matching FSD observations as highlighted

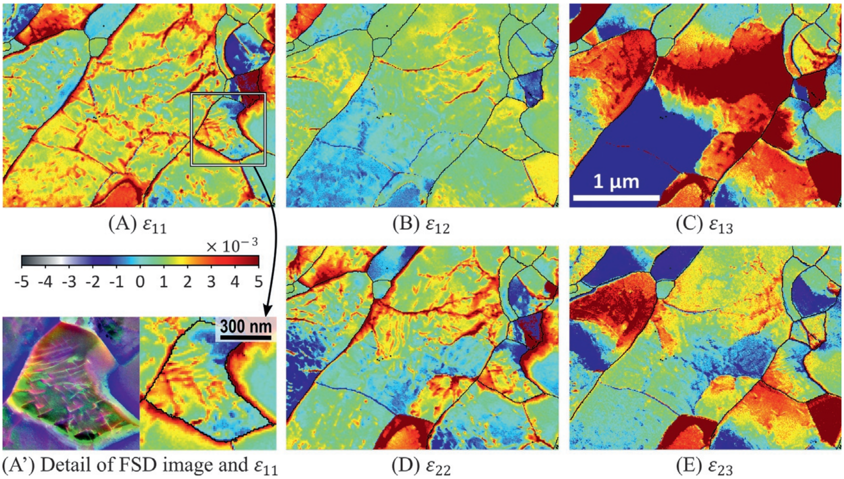

Fig. 6 Elastic strain mappings in ODS steel. The ε_{33} component is not computed, the traction-free surface assumption being questionable due to the presence of near-surface precipitates.

by the close-up in Fig. 6A'. Note that ε_{33} map is absent. Indeed, the traction-free surface condition is not considered here since the material contains surface-near nanoprecipitates (Hardin et al., 2015).

Good agreement is observed in Fig. 4 between the disorientation angle obtained by HTI, the GCC-based initial guess alone or the HR-TKD analysis. Only the roughly triangular grain in the right side of the map shows discrepancies up to $\sim 2°$. The GCC-based initial guess (Fig. 4C) suggests the disorientation angle is underestimated by indexing (Fig. 4A) and overestimated by HR-TKD. Patterns are of relatively poor quality in this grain. The measured elastic strains clearly exceed the elastic limit of the material, which disturbs the determination of rotations and can explain this overestimation.

3.2 HR-EBSD analysis in 15% deformed IF steel

3.2.1 Material and acquisition parameters

An IF steel sheet is deformed by 15% in uniaxial tension testing and characterized by EBSD. The surface is polished manually with abrasive SiC #1600 paper before using diamond polishing suspension containing particles of size 9 μm and 3 μm. Colloidal silica suspension is used as final polishing.

The acquisition parameters are summarized in Table 2. Patterns of 600×600 pixels (Fig. 7A) are acquired by averaging two frames with an exposure time of 75 ms each. This is still particularly short as compared to exposure times encountered in the literature: 2000 ms (Maurice, Driver, & Fortunier, 2012; Wilkinson, Meaden, & Dingley, 2006a) or 3×350 ms (Shi, Roux, & Hild, 2019) for instance. The used SEM lacks stability. Drift becomes visible as horizontal lines in the GND density mappings when setting a longer exposure.

Dead pixels are filtered, and the continuous background is subtracted with a logarithmic high-pass filter of size 51 pixels before reducing noise with a Gaussian filter of radius 1 pixel (Fig. 7B). Dust and a fiber deposited on the scintillator are hidden by applying a mask on the lowest intensities and by defining a circular region of 55 pixels in diameter (highlighted in red), respectively. Note that the pattern displayed is the reference of one the most internally disoriented grain within the map.

Three initial guess strategies are studied through this application. The first one is based on indexing. The two others are the partial and the complete initializations of the homography from the GCC-based method

Table 2 Acquisition parameters of the EBSD dataset in 15% deformed IF steel.

EBSD configuration	
Working distance (*WD*)	15.26 mm
Sample-to-detector distance (*DD*)	16.29 mm
Sample tilt	70°
Detector tilt	−5.4° (with respect to the vertical)
Orientation map	
Magnification	×1600
Step size	220 nm
Map size	$72.2 \times 54.2\,\mu m^2$ (79,376 points)
Pattern acquisition	
Accelerating voltage	20 kV
Probe current	7.1 nA (largest aperture: 120 μm)
Pattern resolution	600 × 600 pixels (pixel size: 40 μm)
Exposure time	75 ms
Frame averaging	2

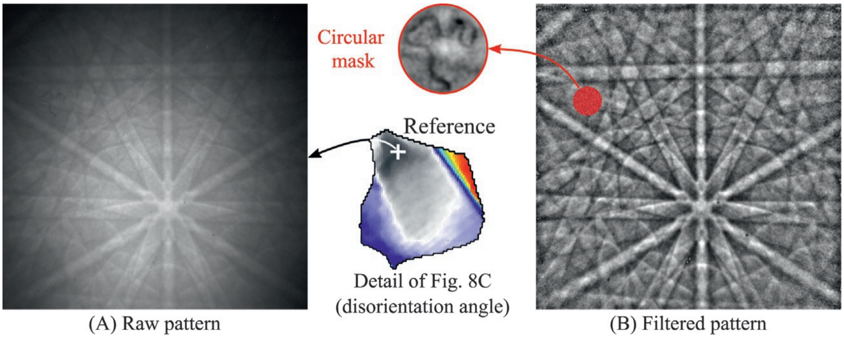

Fig. 7 (A) Raw and (B) filtered reference pattern of the most disoriented grain in the IF steel dataset.

(sections 4.1.2 and 4.2.4 in Chapter "Implementing the homography-based global HR-EBSD/TKD approach" by Ernould et al.). The patterns are pre-aligned from a square region of size 512 × 512 pixels, while a circular region of radius 245 pixels is considered by the IC-GN algorithm.

3.2.2 Grain internal disorientation and GND mappings

The grain internal disorientation angle and the entrywise norm of the Nye tensor obtained from indexing (Fig. 8A,B) are faced to those measured by HR-EBSD after a complete initialization of the homography from

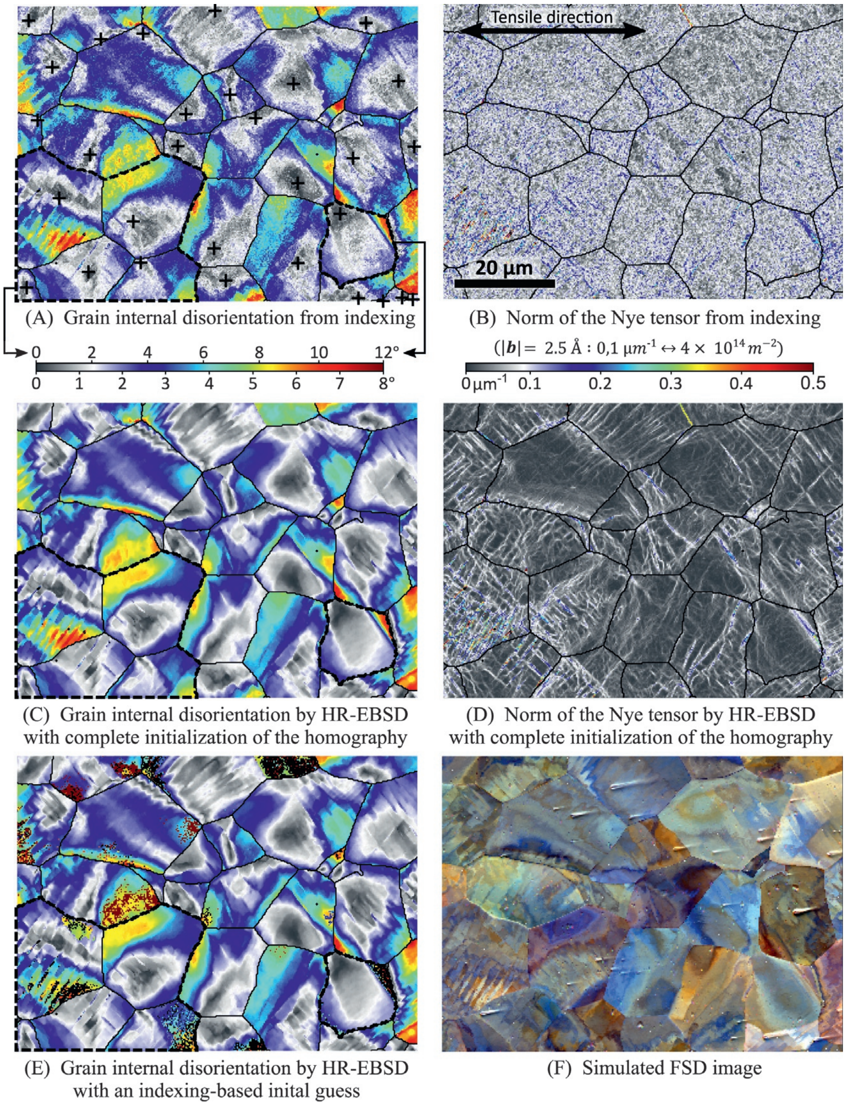

Fig. 8 Grain internal disorientation angle and entrywise norm of the Nye tensor derived (A, B) from indexing and (C, D) by HR-EBSD with a complete initialization of the homography according to GCC-based measurements. Black crosses in (A) indicate the reference of each grain. (E) Disorientation angle by HR-EBSD when using an indexing-based initial guess. (F) Virtual FSD image.

CGG-based measurements (Fig. 8C,D). For better color visualization, the disorientation angle is plotted between 0 and 8° except in the regions outlined by black dashed lines. The latter are subject to larger disorientations and the scale is thus extended to 12°.

Like with the ODS steel, the benefits of the proposed method are particularly visible in terms of GND density. The entrywise norm of the Nye tensor in Fig. 8D is calculated from its assessable components in Fig. 9, in which the left column shows the α_{i3} ($i = [\![1;3]\!]$). These components are fully known as explained in Section 3.1.2. In such a plastically deformed material, the contribution of elastic strains is usually marginal (Jiang, Britton, & Wilkinson, 2015; Wilkinson & Randman, 2010), as illustrated by the contribution of elastic strains to α_{13} in Fig. 9D. Therefore, α_{12} and α_{21} components in Fig. 9E,F are relevant, despites the two-dimensional nature of the measurement prevents elastic strains to be accounted for.

The indexing-based and the GCC-based initial guesses lead to the same results, except in some cases (7.4% of the map), where the indexing-based strategy leads to a divergence or convergence of the IC-GN algorithm to an ostensibly wrong local optimum. Divergence is materialized by black pixels in Fig. 8E and motivated the development of the GCC-based method, as explained in section 4.1.3 in Chapter "Implementing the homography-based global HR-EBSD/TKD approach" by Ernould et al.

Finally, an FSD image is simulated in Fig. 8F. It is computed in the same way as an FSD detector in practice. The intensities of three regions distributed in the lower third of raw patterns (as shown in fig. 5 in Chapter "Measuring elastic strains and orientation gradients by scanning electron microscopy: Conventional and emerging methods" by Ernould et al.) are integrated and each of the so-obtained values is associated with a color channel (blue, green, or red). It is to be compared qualitatively to the HR-EBSD mappings.

3.2.3 Performances of the global cross-correlation based initial guess

3.2.3.1 Influence on initial and final residuals

To remember, the residuals are the differences in intensity between the reference and the target subsets, as defined in eq. (17) in Chapter "Implementing the homography-based global HR-EBSD/TKD approach" by Ernould et al.. In the following, they are multiplied by $\sqrt{N-1}$, where N is the number of points forming the subset, so that it is easier to interpret them (the average and standard deviation of the reference subset and the target subset are thus 0 and 1, respectively).

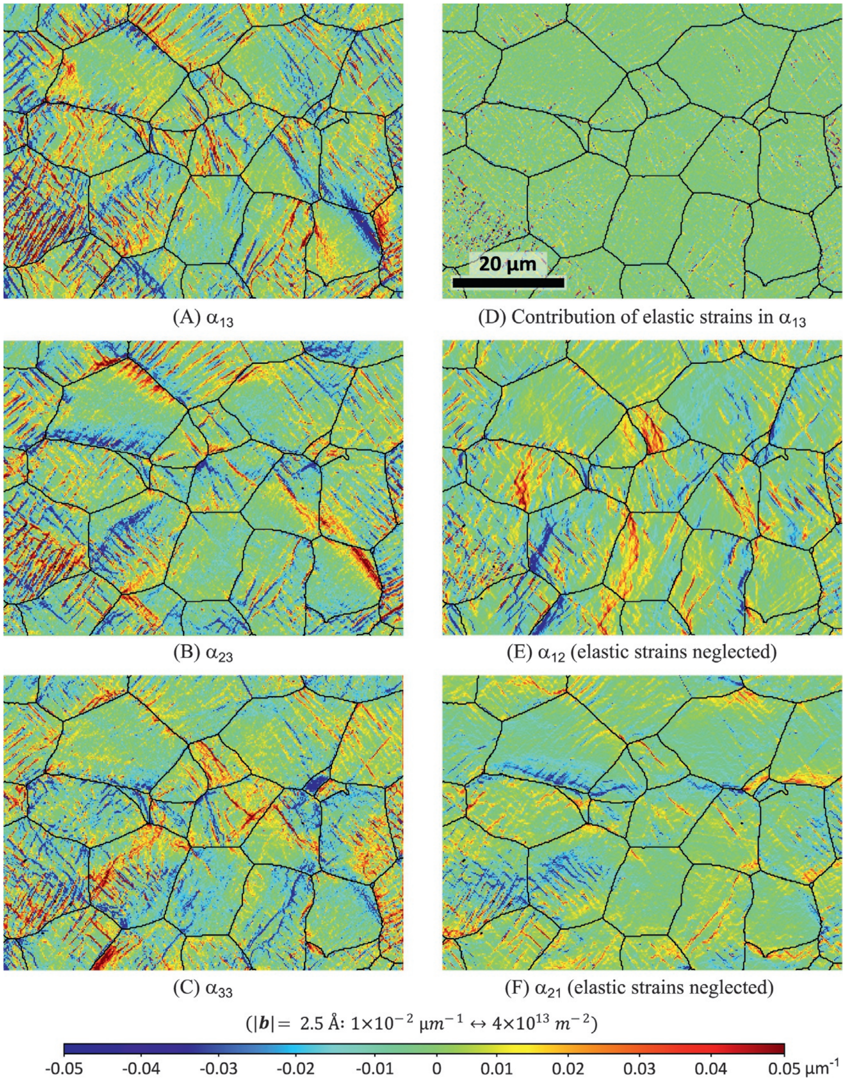

Fig. 9 (A, B, C) α_{13}, α_{23} and α_{33} components of the Nye tensor. They account for the contribution of both curvatures and elastic strains. (D) aElastic strain contribution in the α_{13} component. (E, F) α_{12}, α_{21} components computed from the curvatures only because the contribution of elastic strain is not fully computable.

For each one of the ~79,000 points within the dataset, the average

$$\mu = \frac{1}{N}\sum_{i=1}^{N} \left|\delta\left(\boldsymbol{X}^{(i)}\right)\right| \tag{11}$$

and the standard deviation

$$\sigma=\sqrt{\frac{1}{N}\sum_{i=1}^{N}\left(\left|\delta\left(\boldsymbol{X}^{(i)}\right)\right|-\mu\right)^{2}}, \tag{12}$$

of the absolute residuals $|\delta|$ over the subset are computed at the beginning (initial residuals) and at the end (final residuals) of the IC-GN algorithm. The distribution of μ is plotted in Fig. 10B. Dash-lines and solid lines are associated with initial and final residuals, respectively. The colors indicate the initial guess strategy. Note that the distribution of σ is not displayed because it follows a very similar trend to that of μ.

Partial or complete homography initializations from the GCC-based measurements lead to identical final residuals (superimposed black and blue lines in Fig. 10B,C). Final residuals are higher when using an indexing-based initialization (red) due to divergence of the IC-GN algorithm at some points. Divergence explains the presence of slight peaks around 0.8 and 1 in the μ

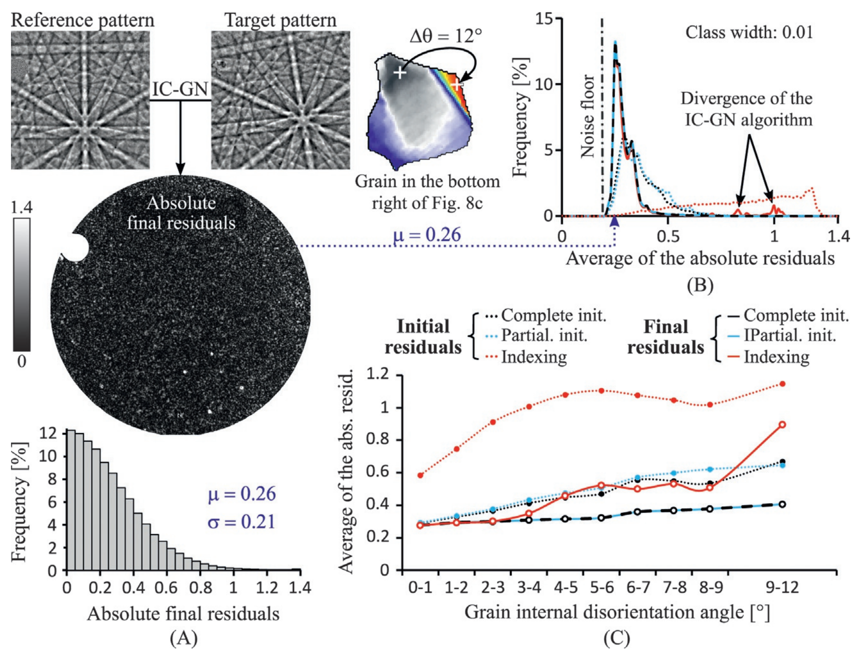

Fig. 10 (A) Image of the final absolute residuals along with their distribution in the case of a complete initialization from the GCC-based measurements. This example considers one of the most disoriented points in the map ($\Delta\theta \approx 12°$). (B) Distribution of the average of the initial and final absolute residuals for different initialization strategies. (C) Average of the absolute residuals as a function of the grain internal disorientation angle.

distribution, as indicated by arrows in Fig. 10B. In all cases, the average of the final absolute residuals is always greater than 0.2. This is attributable to noise. Indeed, Fig. 10A shows the final absolute residuals between two of the most disoriented patterns in the map. They do not reveal any particular misalignment after image registration while their average value (0.26) is representative of the dataset, as indicated by the blue arrow in Fig. 10B.

Regarding the average of the initial absolute residuals (dash-lines curves in Fig. 10C), it is twice lower for the proposed GCC-based method (blue and black) than for the indexing-based initial guess (red). The partial homography initialization leads to initial absolute residuals having a higher average than with a complete initialization. This is because the latter better account for of gnomonic distortions, as illustrated in fig. 13 in Chapter "Implementing the homography-based global HR-EBSD/TKD approach" by Ernould et al.

3.2.3.2 Angular deviation between the initial guess and the solution

The true solution being unknown, lattice rotations determined by HR-EBSD following a complete initialization of the homography from GCC-based measurements are taken as reference. This reference is denoted as the solution in the following. Differences in lattice rotations or disorientation angle between the initial guess and this solution are called angular deviations, or absolute angular deviations when reasoning in absolute value.

First, the distribution of the angular deviation on the disorientation angle is plotted in Fig. 11A. The indexing-based initial guess, in red, shows a twice higher standard deviation as compared to the GCC-based one, in black (0.44° versus 0.22°, respectively). No distinction is made between the partial

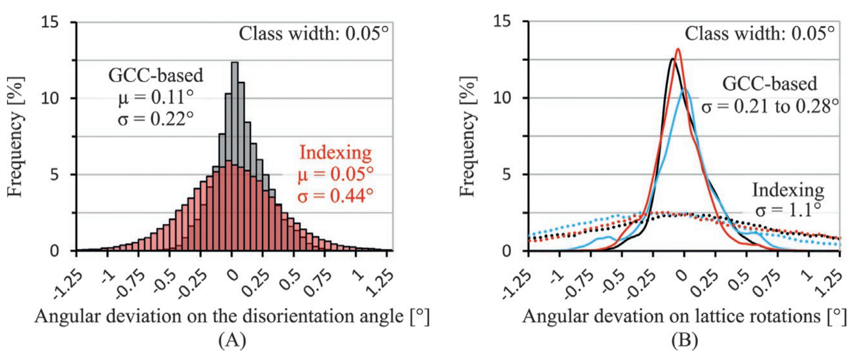

Fig. 11 (A) Distribution of angular deviations on the disorientation angle between the initial estimate and the solution. (B) Distributions of angular deviations on lattice rotation δw_{ij}.

or complete initializations as the estimation of rotations is just the same. It only depends on GCC measurements. Both distributions are centered on the solution within 0.1°, with a slight overestimation of disorientations by the GCC-based approach as compared to indexing (0.11° versus 0.05°, respectively).

Beyond the disorientation angle, the disorientation axis is also important, especially since it must be known to warp the initial target subset correctly. Lattice rotations with respect to each axis of the basis are displayed in Fig. 11B. Overall, angular deviation between the initial guess and the solution is about 1° for indexing (dotted lines). Although disorientation angle derived from HTI is mostly estimated within ~0.5° (Fig. 11A), which is in line with literature, the disorientation axis lacks accuracy. Benefits of the proposed GCC-based approach are illustrated by the narrower distributions in Fig. 11B (solid lines), whose standard deviation is 0.21°, 0.22° and 0.28° for rotation w_{21}, w_{23} and w_{13}, respectively. The larger error observed with the latter component is consistent with the numerical validation in Chapter "Numerical validation and influence of optical distortions on accuracy" by Ernould et al. (section 3.2.2). The horizontal shift measured is here affected by the more pronounced asymmetry of gnomonic distortions between the top and bottom of the patterns. Rotation w_{13} may be responsible for the above-mentioned overestimation of the disorientation angle by the GCC-based method.

3.2.3.3 Consequences on convergence speed of the IC-GN algorithm

Fig. 12A shows the distribution of the number of iterations for each of the three initialization strategies. As compared to a complete initialization, a

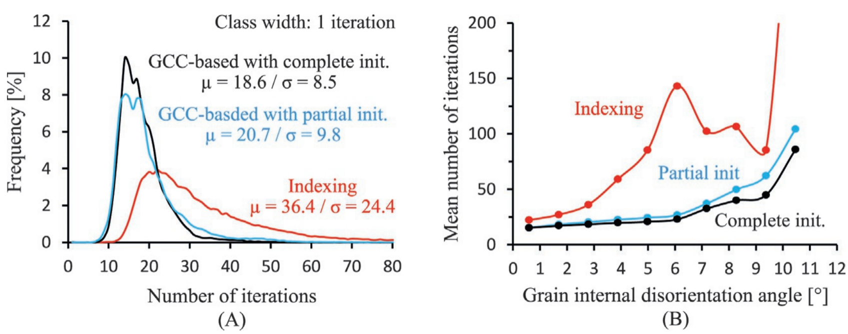

Fig. 12 (A) Distribution of the number of iterations of the IC-GN algorithm for different initial guess strategies. μ and σ denote the average and standard deviation of a distribution, respectively. (B) Number of iterations as a function of the grain internal disorientation angle.

partial initialization and an indexing-based initialization require ∼11% and ∼96% more iterations in average, respectively. Thus, the numerical cost of the pattern pre-alignment method is offset by the approximately twice as fast convergence of the IC-GN algorithm in this example.

For all initial guess strategies, the average number of iterations increases with the disorientation angle in Fig. 12B. These results are correlated with the average of the initial absolute residuals in Fig. 10C. When using an indexing-based initial guess, the IC-GN algorithm diverges almost systematically from 9° of disorientation. The GCC-based method ensures a reasonable convergence of the IC-GN algorithm for the whole range of disorientation studied. Nevertheless, it should be noted that in cases where the disorientation reaches 12°, lattice rotation is mainly carried by w_{21} (∼9°), as visible from the patterns in the top left corner of Fig. 10.

3.3 Characterization of a deformed nanostructure in the SEM

For this last application in a deformed metal, nanocrystalline aluminum obtained by severe plastic deformation (Estrin & Vinogradov, 2013) is investigated by on-axis TKD. Objective is to highlight the ability of on-axis HR-TKD to provide simultaneous high-spatial and high angular resolutions. The interest of FSD imaging is also discussed in the light of bright-field imaging in the transmission electron microscope (TEM).

3.3.1 Material and acquisition parameters

A thin foil of pure aluminum that has undergone ten passes of equal channel angular extrusion is obtained by twin jet electropolishing. The smallest available aperture (20 μm) is selected to optimize image sharpness of FSD imaging in Fig. 13A–F. At low magnifications (×100, ×1000 and ×4000), FSD imaging mainly provides information on sample thickness. The thinnest areas appear in green while the thickest ones are purple. Regions thin enough to acquire Kikuchi patterns are thus easily identified. At higher magnifications (×16,000 and above), the sample thickness is assumed constant over the observed area. Color variations correspond then essentially to an orientation contrast, chemical contrast being absent in pure aluminum.

A region of approximately 1.3 μm^2 is first mapped with 6.5 nm step size at ×95,000 magnification (Fig. 13F). Acquisition parameters are summarized Table 3. The analyzed area is composed of elongated grains. They contain subgrain boundaries along their transverse direction, which is about 50 to

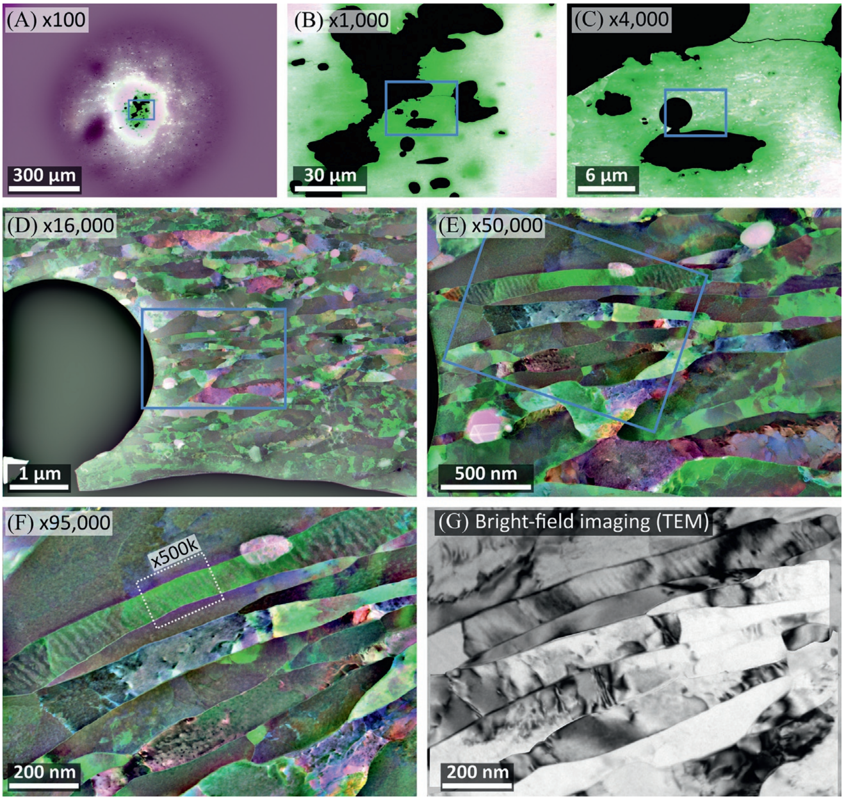

Fig. 13 FSD imaging at several magnifications of nanocrystalline aluminum obtained by severe plastic deformation and comparison with bright field imaging in the TEM.

200 nm wide, as shown by sudden color changes. From this standpoint, FSD contrast is easier to interpret than the black and white bright-field image by TEM in Fig. 13G. This is especially true since the latter image is actually a patchwork of several TEM images acquired at different sample tilt angles. It should be pointed out, however, that TEM imaging is here suffering from contamination of the foil during the previous on-axis TKD analyses.

One of the grains shows striations. They will be characterized by making a second map with a step size of 3 nm at a magnification of ×500,000. The acquisition parameters are summarized in Table 4 and the location of the analyzed region is delimited by a white dotted line in Fig. 13F.

For both maps, 600 × 600-pixel patterns are recorded. They are filtered in a way similar to the ODS steel. Fig. 14 shows the reference pattern of the striated grain reference pattern after filtering for each of the two maps

Table 3 Acquisition parameters of the on-axis TKD dataset in nanocrystalline aluminum at a magnification of ×95,000.

On-axis TKD configuration	
Working distance (WD)	6.9 mm
Sample-to-detector distance (DD)	18.8 mm
Sample tilt	0°
Detector tilt	0.325° (with respect to the horizontal)
Orientation map	
Magnification	×95,000
Step size	6,5 nm
Map size	$1.309 \times 0.959\,\mu m^2$ (25,619 points)
Pattern acquisition	
Accelerating voltage	30 kV
Probe current	1.25 nA (central aperture: 60 μm)
Pattern resolution	600 × 600 pixels (pixel size: 40 μm)
Exposure time	95 ms
Frame averaging	2

(×95,000 and ×500,000). A 512 × 512-pixel square subset is used for the GCC-based initial guess. A circular subset of radius 241 pixels (×95,000) and 211 pixels (×500,000) is considered during subpixel registration.

3.3.2 Grain internal disorientation, GND and elastic strains mappings

Fig. 15 compares the grain internal disorientation and entrywise norm of the Nye tensor derived from indexing and by on-axis HR-TKD. White crosses in Fig. 15A spot the location of the reference of each grain. Differences in noise and sensitivity of GND densities are like those already observed for the ODS or IF steel datasets. The on-axis HR-TKD technique allows the quantification of GND densities at subgrain boundaries disoriented by several degrees, but also to visualize the emergence of dislocation structures associated with low-angle grain boundaries (<2°), consistently with details in the FSD image.

Table 4 Acquisition parameters of the on-axis TKD dataset in nanocrystalline aluminum at a magnification of ×500,000.

On-axis TKD configuration	
Working distance (WD)	1.9 mm
Sample-to-detector distance (DD)	24.4 mm
Sample tilt	0°
Detector tilt	0.325° (with respect to the horizontal)
Orientation map	
Magnification	×500,000
Step size	3 nm
Map size	0,291 × 0,102 μm^2 (3289 points)
Pattern acquisition	
Accelerating voltage	30 kV
Probe current	1.25 nA (central aperture: 60 μm)
Pattern resolution	600 × 600 pixels (pixel size: 40 μm)
Exposure time	25 ms
Frame averaging	3

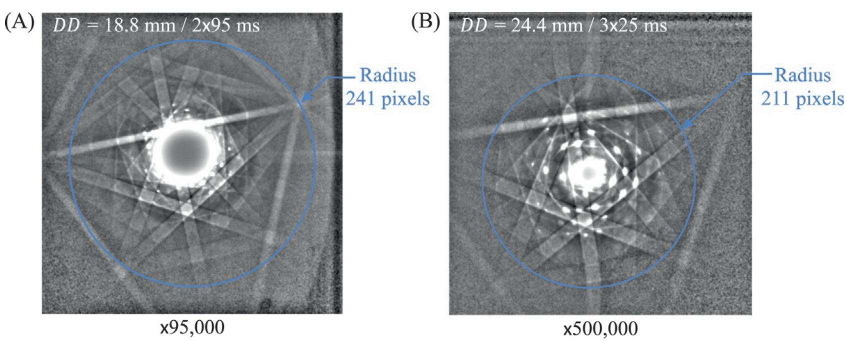

Fig. 14 Filtered reference pattern of the striated grain adapted from the datasets acquired at (A) ×95,000 and (B) ×500,000.

The SEM is now pushed to its limits in order to characterize the striated grain in Fig. 13F. When observed by FSD (Fig. 16A) or in bright-field in a TEM (Fig. 16B), these striations appear as diffuse domains of about 25 nm wide. In particular, no dislocations are visible in the TEM image. In

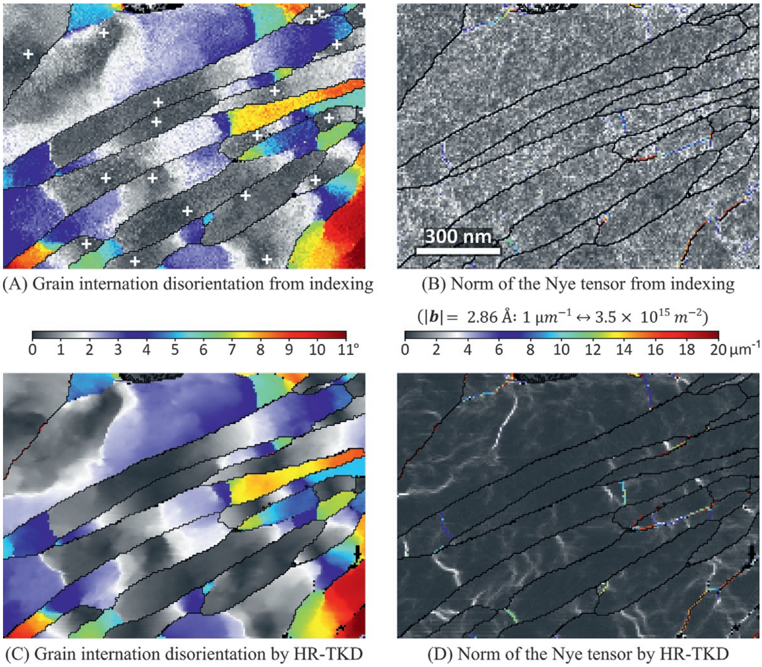

Fig. 15 Grain internal disorientation angle and entrywise norm of the Nye tensor derived (A, B) from indexing and (C, D) by HR-TKD with a complete initialization of the homography according to GCC-based measurements. White crosses in (A) indicate the reference of each grain.

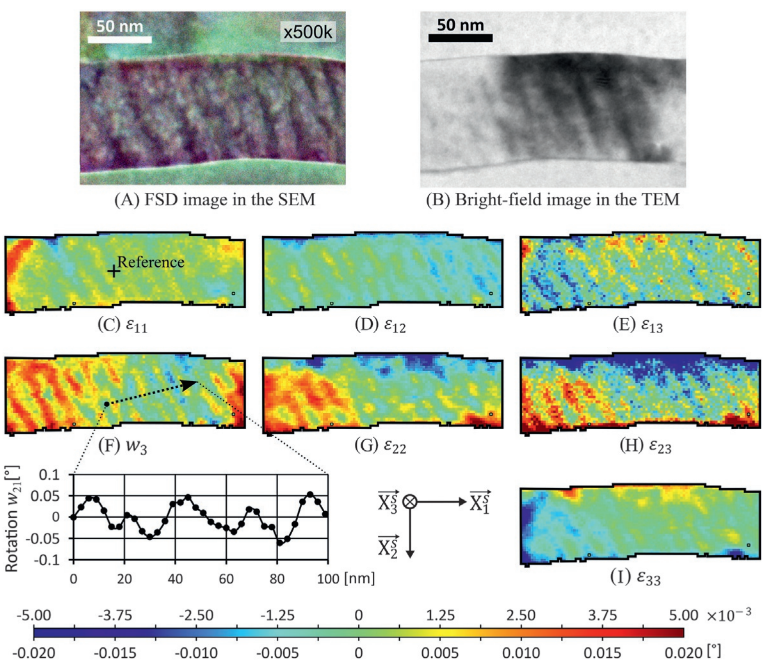

Fig. 16 (A) FSD imaging in the SEM and (B) bright-field imaging in the TEM of a detail in the striated grain. (C–I) Elastic strain components and rotation w_{21} accompanied with a profile.

agreement, the GND density obtained by HR-TKD is zero in this region in Fig. 15D. Similar striations are observed in the elastic strain maps by on-axis HR-TKD. Rotations w_{32} and w_{13} are not displayed for the sake of space, as they do not show any trend, unlike w_{21} in Fig. 16F from which a profile is extracted. It suggests the angular resolution is close to 0.01°.

4. Elastic strain measurement in semiconductors

The previous examples tackled the measurement of orientation gradients for the calculation of GND densities in plastically deformed metals. This section focuses on measuring elastic strains in semiconductors. Elastic strains of the order of 2% associated with the parametric mismatch between a silicon substrate and a germanium enriched layer are first investigated by on-axis HR-TKD. A GaN single crystal containing disoriented domains of the order of a tenth of a degree is then analyzed by HR-EBSD.

4.1 On-axis TKD analysis in $Si_{0,69}Ge_{0,31}$ epitaxial layer on Si substrate

4.1.1 Material and acquisition parameters

The thin foil, courtesy of Dr. Jean-Luc Rouvière from CEA Leti, is imaged by FSD in Fig. 17A. It contains a 28.5 nm wide $Si_{0.69}Ge_{0.31}$ layer highlighted by a red dash line. It is obtained by epitaxial growth along its longitudinal direction on a silicon substrate. The interface between this layer and the substrate has a normal aligned with the [001] direction of silicon, as schematized by a lattice cell in Fig. 17B. The latter FSD image, acquired at ×300,00 magnification, mainly shows chemical contrast. The germanium enriched

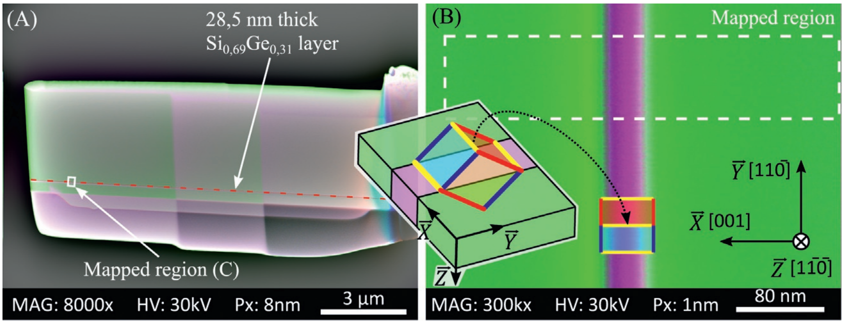

Fig. 17 (A) FSD image of the silicon foil containing an epitaxial germanium enriched highlighted by the red dash line. (B) FSD observation of the layer at ×300,000 magnification and scheme of its lattice cell orientation relative to silicon.

Table 5 Acquisition parameters of the on-axis TKD dataset in $Si_{0,69}Ge_{0,31}/Si$.

On-axis TKD configuration	
Working distance (WD)	1.70 mm
Sample-to-detector distance (DD)	23.85 mm
Sample tilt	0°
Detector tilt	0.025° (with respect to the horizontal)
Orientation map	
Magnification	×300,000
Step size	3 nm
Map size	$0.373 \times 0.077\ \mu m^2$ (12,096 points)
Pattern acquisition	
Accelerating voltage	30 kV
Probe current	1.25 nA (central aperture: 60 μm)
Pattern resolution	1200 × 1200 pixels (pixel size: 20 μm)
Exposure time	120 ms
Frame averaging	1

layer is in purple, and silicon appears in green. The uniform colors suggest there is no orientation change nor chemical heterogeneity (except at the interface).

Table 5 details the acquisition parameters of the on-axis TKD delimited by a white dashed line in Fig. 17B. Low probe current and maximum acceleration voltage are used to improve spatial resolution as much as possible, the step size being 3 nm. Since optical focusing on a single crystal is difficult, the specimen is brought very close to the polar piece in the event the electron beam is slightly divergent. This also increases the sample-to-detector distance, which favorized the angular sensitivity of the HR-TKD technique. In addition, patterns are recorded using the largest resolution possible, namely 1200 × 1200 pixels.

Patterns are filtered by applying a logarithmic high-pass filter of size 71 pixels followed by a Gaussian filter of radius 2 pixels (Fig. 18A). Unfortunately, white balance between both side of the detector is inequal. The left side is brighter as illustrated by the green-delimited close-up. This

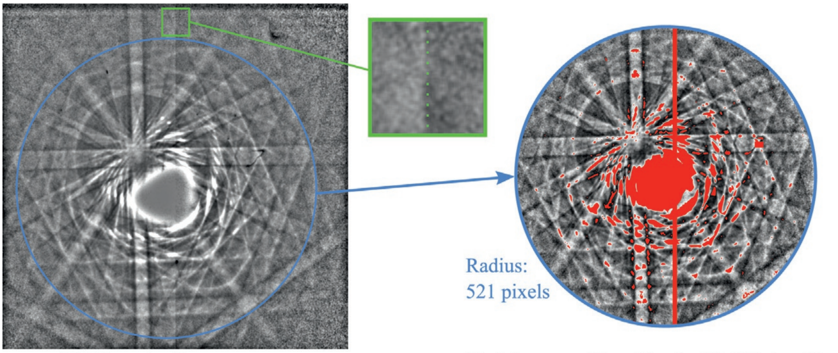

Fig. 18 (A) Filtered reference pattern and (B) subset considered by the IC-GN algorithm (red regions do not belong to the subset).

manual setting is particularly difficult, because of the significant intensity dynamic in on-axis TKD raw patterns. A vertical mask is added to prevent the interface between the two halves of the pattern from dealing as an anchor during the DIC analysis (red band in Fig. 18B). The IC-GN algorithm is applied considering a circular region of radius 521 pixels centered at $\boldsymbol{X_0} = [568 \;\; 670]^T$ (Fig. 18B).

4.1.2 Elastic strain profiles

Elastic strains are expressed in a frame, whose X and Y directions are collinear with [001] and $\left[1\bar{1}0\right]$ directions of $Si_{0.69}Ge_{0.31}$. Profiles in Fig. 19A are adapted from (Béché, 2009), who characterized a similar specimen using nanobeam electron diffraction (NBED) in the TEM. They are to be compared with those by on-axis HR-TKD in Fig. 19B.

Elastic strains by HR-TKD in Fig. 19B corresponds to a 280 nm long profile, whose position within the scan is indicated by a black arrow in the ε_{xx} map in Fig. 19C. The black cross spots the reference, whose pattern is displayed in Fig. 18A. It is selected away from the $Si_{0.69}Ge_{0.31}$ layer to be assumed strain-free (note that ε_{xx} is constant in the reference neighborhood).

Lattice parameter of silicon and germanium is $a_{Si} = 0.5431$ nm and $a_{Ge} = 0.5657$ nm, respectively. From these values, lattice parameter of $Si_{x-1}Ge_x$ is deduced (de Gironcoli, Giannozzi, & Baroni, 1991):

$$a_{SiGe}(x) = a_{Si} + 0.02005.x + 0.00263.x^2. \tag{13}$$

For $x = 0.1$, Eq. (13) yields $a_{SiGe} = 0.5495$ nm. Hence, the misfit with respect to the silicon substrate,

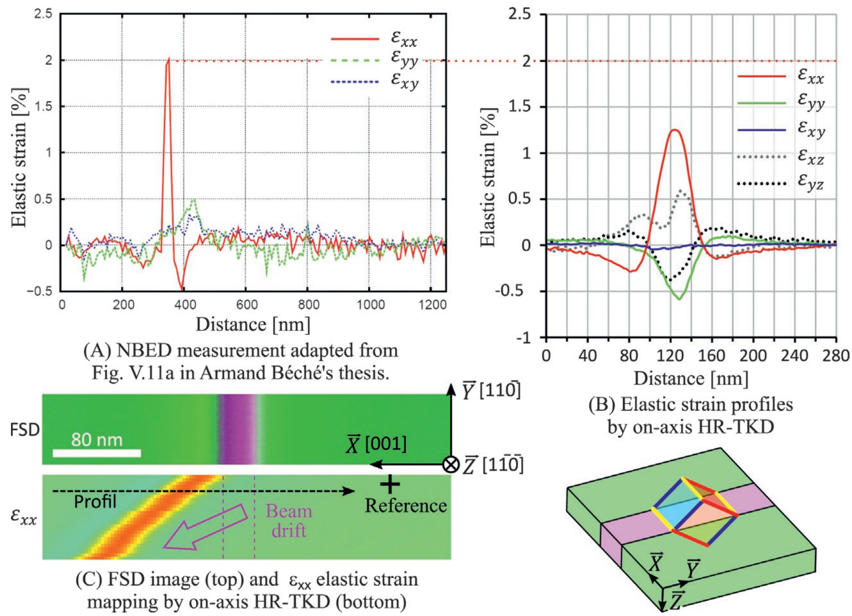

Fig. 19 Elastic strain profiles in $Si_{0.69}Ge_{0.31}$ epitaxial layer measured by (A) NBED in the TEM (Béché, 2009) and compared to (B) on-axis HR-TKD measurements. (C) Mapping of the ε_{xx} component by on-axis HR-TKD highlighting the prominent beam drift during acquisition.

$$f = \frac{a_{SiGe} - a_{Si}}{a_{Si}}, \tag{14}$$

is 0.012. As shown by FSD imaging in Fig. 17A, the substrate width is much larger than the layer's one along its normal direction, so it can be seen as infinite. Based on this, the theoretical dilatation ε_{xx}^{th} is computed as follows (see appendix C.2 in Béché, 2009):

$$\varepsilon_{xx}^{th} = \frac{f}{C_{11}^{SiGe}} \left(2C_{12}^{SiGe} + C_{11}^{SiGe}\right) \tag{15}$$

Material stiffness constants are C_{11}^{SiGe}=154,24 GPa and C_{12}^{SiGe}= 59,06 GPa according to (Levinshtein, Rumyantsev, & Shur, 2001):

$$C_{11}^{SiGe} = 165{,}8 - 37{,}3.x$$

and

$$C_{12}^{SiGe} = 63{,}9 - 15{,}6.x. \tag{16}$$

Finally, it arises ε_{xx}^{th}=2.1%.

The $Si_{0.69}Ge_{0.31}/Si$ thin foil was manufactured to validate the NBED method (Béché, 2009; Béché, Rouvière, Clément, & Hartmann, 2009; Rouviere, Béché, Martin, Denneulin, & Cooper, 2013). The maximum elastic strain measured by this technique in Fig. 19A fits the theoretical value of 2.10%. It is not the case with on-axis HR-TKD, ε_{xx} being only 1,23%. However, HR-TKD measurements should not be directly compared to ε_{xx}^{th}. Both NBED and on-axis HR-TKD measurements were performed with the same step size of 3 nm, but the acceleration voltage is 10 time greater in the TEM, namely 300 kV. The physical meaning of the measured elastic strains is consequently not the same.

On the one hand, the theoretical value considers a bulk specimen. NBED measurements are average values over the entire foil thickness, whereas the diffraction signal in TKD stems from the vicinity of the electron beam outlet surface. At 30 kV, the resolution in depth of TKD is about 65 nm in silicon and 30 nm in germanium (Brodu & Bouzy, 2017), increasing the sensitivity of this technique with stress relaxation at the surface.

On the other hand, the physical spatial resolution is rather 10 nm laterally for on-axis TKD (Niessen et al., 2018; Shen et al., 2019). It is degraded by beam broadening along the sample thickness, while this phenomenon is marginal in the TEM. Finite-elements analysis is therefore necessary to assess ε_{xx} near the surface, but also to convolve numerical simulation results by the size of the diffraction volume. The latter can be estimated by Monte-Carlo simulation. At given primary electron energy, this volume depends on atomic number and sample thickness (Brodu & Bouzy, 2017). Accounting for the probe size is therefore even more important here, as the foil is quite thick for TKD. Moreover, elastic strain gradients are pronounced along the measurement direction X as ε_{xx} changes from ~ 0 to $\sim 2\%$ over only ~ 14 nm of distance (half the width of the enriched layer). This explains the peak in Fig. 19B is about 66% broader than the investigated layer, namely 50 and 30 nm, respectively.

If the gap observed between theory (2.10%) and HR-TKD (1.23%) is consistent, elastic strain profiles in Fig. 19B remain preliminary results. Effort must also be made on calibration. Regarding shear components, ε_{xy} is almost zero along the profile, its extreme values being -4×10^{-4} and 2×10^{-4}. As outlined by (Alkorta, 2013), this component is not affected by uncertainty un the projection geometry, contrary to ε_{xz} and ε_{yz}. For these components, phantom strains of the order of x^*/DD are induced, where x^* is the uncertainty in PC location. Here, this uncertainty is expected to be 0.5% of the pattern width (Villert et al., 2009), i.e., about 6 pixels. Phantom strains of about 5×10^{-3} are potentially present, especially considering possible optical distortions.

Despites all this, it worth noting elastic strain levels away from the $Si_{0.69}Ge_{0.31}$ layer are close to zero. Overall, on-axis HR-TKD profiles are significantly less noisy than those made by NBED. Good repeatability is also observed from one line to another in Fig. 19C (when ignoring beam drift).

This work should be continued using an equipment better suited for high-spatial and high-angular resolutions. Granted, magnification is very large for an SEM (×300,000) but the SEM used is primarily tailored for imaging and sorely lacks stability. Despites efforts to limit beam drift (no frame averaging, no stage movement and high voltage initiated several hours prior measurement), the vertical germanium enriched layer in the FSD image (Fig. 19C) appears tilted by nearly 45° in the ε_{xx} map. The beam drift is extremely marked to the point of affecting the measurement. A shift of 6 to 12 nm is observed between each line of the map in Fig. 19C although the acquisition time of a line is less than 15 s.

4.2 HR-EBSD analysis in GaN single crystal

4.2.1 Material and acquisition parameters

An Si doped GaN standard sample of 3.5 mm thickness deposited by metal organic vapor phase epitaxy on a sapphire substrate is characterized by EBSD. As shown by FSD imaging in Fig. 20A, it contains threading dislocations separating slightly disoriented domains. This application thus focuses on measuring both small elastic strains ($<2\times10^{-3}$) and rotations ($<0.3°$).

The dataset in GaN is courtesy of Dr. Haitehm Mansour, who did his PhD at our lab (Mansour, 2016). Diffraction patterns are acquired using another SEM than in previous examples. It is equipped with an Oxford Symmetry camera, which is optical-distortion free as lenses are replaced by tapered optical fibers. Acquisition parameters are summarized in Table 6. An orientation map of the observed region in Fig. 20A is performed with 40 nm step size, at 15 kV and 10 nA probe current. Note that the sample to detector distance could have been increased, to enhance angular sensitivity.

Pattern resolution is 1244 × 1024 pixels and their signal-to-noise ratio is the highest of all the proposed applications. Raw intensities are divided by those of an image of the continuous background and a Gaussian spatial filter with radius of 1 pixel is applied. The filtered reference pattern is displayed in Fig. 20B, where the considered used by the IC-GN algorithm is plotted in green overlay. It is an ellipse whose major and minor axes are 1135 and 925 pixels, respectively. The traction-free surface condition is applied using the material stiffness coefficients measured by (Polian, Grimsditch, & Grzegory, 1996).

Table 6 Acquisition parameters of the EBSD dataset in GaN single crystal.

EBSD configuration	
Working distance (*WD*)	14.47 mm
Sample-to-detector distance (*DD*)	14.14 mm
Sample tilt	69.99°
Detector tilt	−5.98° (with respect to the vertical)
Orientation map	
Magnification	×12,000
Step size	40 nm
Map size	5.16 × 3,32 μm^2 (10,707 points)
Pattern acquisition	
Accelerating voltage	15 kV
Probe current	10 nA
Pattern resolution	1244 × 1024 pixels (pixel size: 19.6 μm)
Exposure time	100 ms
Frame averaging	3

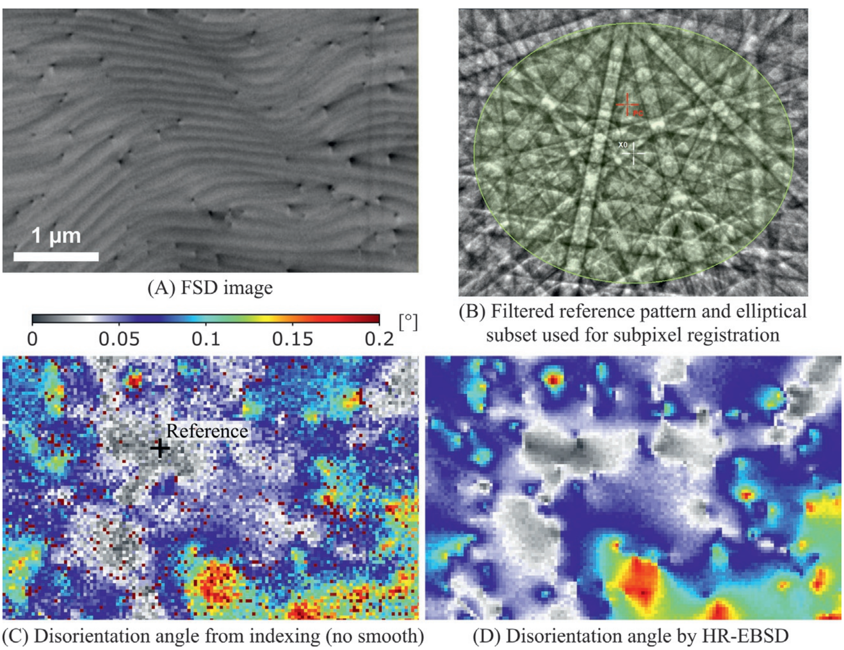

Fig. 20 (A) Images FSD of GND single crystal. Dark spots are threading dislocations. (B) Filtered reference pattern whose location is indicated by black cross in (C) the map of the disorientation angle derived from indexing. (D) Disorientation angle measured by HR-EBSD.

Since low disorientations are expected according to indexing Fig. 20C, the homography is simply initialized as the identity matrix. Actually, further analyses with the GCC-based method yield the same HR-EBSD results. Apart from some outliers involving disorientations about 0.2 to 0.4°, indexing by Aztec-software catches disorientations as low as 0.05°, consistently with HR-EBSD measurements in Fig. 20D. Here, the refined-accuracy mode is enabled. The resolution of the Radon-transform is refined in the vicinity of detected peaks associated with Kikuchi bands in the Hough-space (see section 2.4.1 in Chapter "Measuring elastic strains and orientation gradients by scanning electron microscopy: Conventional and emerging methods" by Ernould et al.). Branches of hyperbola are also accounted for when fitting Kikuchi bands.

4.2.2 Results of the HR-EBSD analysis

Elastic strain and rotation mappings by HR-EBSD are plotted in Fig. 21. Elastic strain components are in the range $\pm 1 \times 10^{-3}$. Overall, ε_{i3} elastic strain components (right column) are close to zero, which supported the

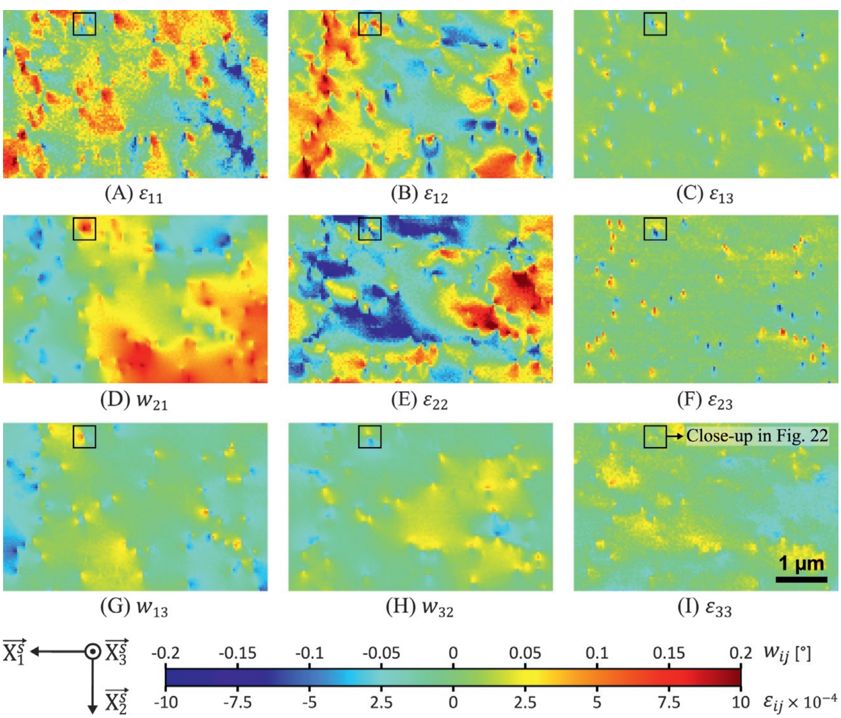

Fig. 21 Elastic strains and lattice rotations measured by HR-EBSD.

validity of the traction-free surface assumption. Out-of-plane shear components ε_{13} and ε_{23} are non-zero very locally, i.e., where threading dislocations are visible in the FSD image (Fig. 20A). Regarding rotations, disoriented domains observed in Fig. 20B are primarily tilted with respect to the surface's normal. Indeed, rotation w_{21} in Fig. 21C reaches up to 0.2° while the two other components are mostly below 0.05° in absolute value.

The sensitivity of the proposed HR-EBSD approach is sufficient to highlight distortion fields in the vicinity of dislocation cores. Fig. 22 proposes a close-up of the mappings in Fig. 21 in the vicinity of a threading dislocation (Fig. 22J). One can see lobes, in the manner of a clover. They are highlighted by black lines drawn manually. Both the shapes and signs are similar to theoretical elastic strain and rotation fields induced by a screw dislocation line near a free surface, as can be simulated using dislocation models (Eshelby & Stroh, 1951) or piezoelectric dislocation frameworks (Han & Pan, 2012; Shi, Asbeck, & Yu, 1999; Taupin, Fressengeas, Ventura, Lebyodkin, & Gornakov, 2014).

The components of the Nye tensor and its entrywise norm are displayed in Fig. 23. The sensitivity of GND densities is better than 5×10^{-3} μm^{-1}, which is 1×10^{13} m^{-2} at 40 nm step size when considering a magnitude of the Burgers vector of 0.52 nm. All threading dislocations visible in the FSD image (Fig. 23A) can be found in α_{12} and α_{21} mappings (Fig. 23B,D). The latter do not account for elastic strains, unlike α_{i3} components (Fig. 23C,E, G). Similarly to the application in IF steel (Fig. 9D), α_{13} is taken as an example again, to discuss the relative importance of the contributions of lattice

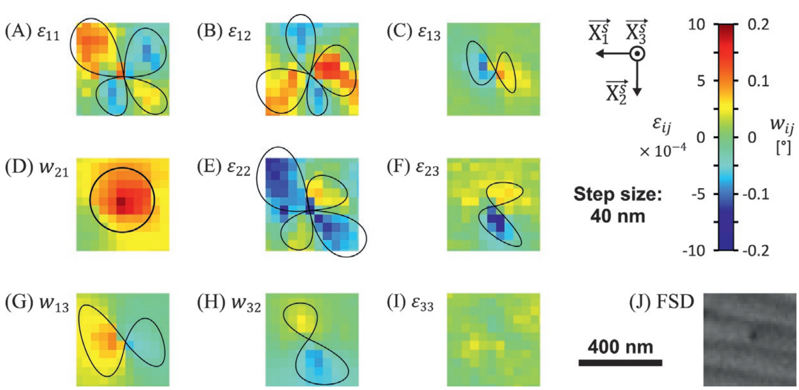

Fig. 22 Close-up of elastic strain and rotations mappings in Fig. 21 in the vicinity of a threading dislocation, and corresponding FSD image adapted from Fig. 20A. Black lines are drawn manually to highlight the trend.

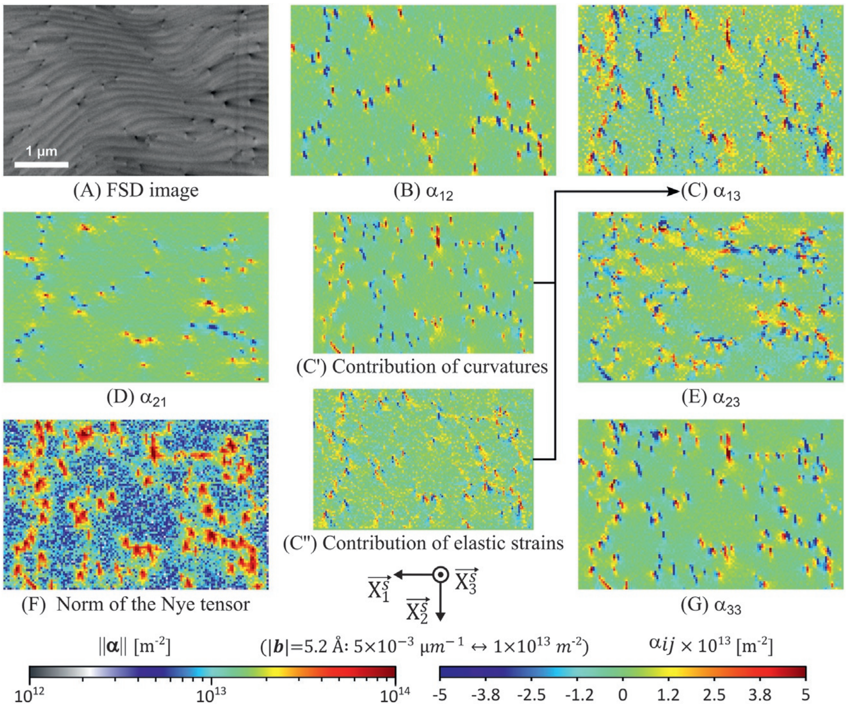

Fig. 23 (A) FSD images where threading dislocations are faithfully recovered by the HR-EBSD analysis according to (B–E,G) the components of the Nye tensor or (F) its entrywise norm. The contributions of (C′) lattice curvatures and (C″) elastic strains regarding (C) the α_{13} component shows that the latter is not negligible at such low disorientations.

curvatures and elastic strains to GND densities. These contributions are plotted separately in Fig. 23C' and C'', respectively. The magnitude of curvatures is typically 4–5 $\times 10^{13}$ m^{-2} near dislocation core, while it is about 3×10^{13} m^{-2} for $\boldsymbol{curl}(\boldsymbol{\varepsilon})$. Neglecting elastic strains is thus no longer acceptable in the presence of disorientations about 0.1°.

In order to better quantify the resolution of the technique on lattice rotations and elastic strains, differences between adjacent pixels are computed along the rows and columns of the map. Then, the standard deviation of these differences is computed for each component. In average, it is 1.0×10^{-4}, and the maximum and minimum are 1.4×10^{-4} and 6.1×10^{-5}, respectively. Actually, values are distributed into two groups. The standard deviation is 1.1–1.4 $\times 10^{-4}$ for all rotation and in-plane strain components while it is about 7.0×10^{-5} for the remaining components (ε_{13}, ε_{23}, ε_{33}). However, the calculation is biased as it is not possible to discriminate between measurement noise and the actual variation in the material. This explains the largest standard deviations are associated with the components having in overall the highest magnitude in Fig. 21. Moreover, the relative importance of these two contributions depends on the step size.

Here, step size is 40 nm. Since it is close to the limit of the HR-EBSD technique, the contribution of noise is preponderant. Nevertheless, the step size remains quite large when considering the very localized distortions caused by threading dislocations. Therefore, differences between neighboring pixels and their standard deviation are recomputed, but pixels where the norm of the Nye tensor is larger than 3×10^{-13} m^{-2} are ignored (orange or red regions in Fig. 23F). Now, standard deviation is in average 7.5×10^{-5} when considering all components. The highest standard deviation is 1.1×10^{-4} for ε_{11}, then it is between 7 and 9×10^{-5} for rotations and other in-plane strain components, and between 5 and 3×10^{-5} for out-of-plane strain components. A resolution of at least 1×10^{-4} on lattice rotations and elastic strains is therefore a reasonable claim.

5. Discussion

Performances of the proposed global HR-EBSD/TKD approach are illustrated through various applications, both from the point of view of the material and of the characterization technique. The method is applied to semiconductors as well as to plastically deformed polycrystalline metals, using both EBSD and on-axis TKD techniques. This section first reviews the main results and highlights the originality of these applications. The on-axis HR-TKD technique is then specifically discussed in the light of TEM-based techniques.

5.1 Main results and originality

From its origin (Troost, Sluis, & Gravesteijn, 1993; Wilkinson, 1996, 1997), the HR-EBSD technique is typically applied to semiconductors to assess its accuracy. Si_xGe_{1-x} or Si are particularly used. Here, GaN single crystal is used as a model material. The elastic strain state being unknown, no claim in accuracy is, however, intended, rather sensitivity. The latter appears better than 1×10^{-4}, in line with literature. This enables to catch distortions caused by some isolated dislocations, as shown in Fig. 22. Those dislocations are also clearly visible in GND density mappings in Fig. 23, which are particularly noise sensitive as their computation involves spatial derivates (see Section 2.3).

The lateral resolution of EBSD limits threading dislocation to be finely observed. Nevertheless, the proposed method is promising for the study of larger defects, like nanopipe or giant screw dislocations (Pirouz, 1998). Recently, (Yu, Liu, Karamched, Wilkinson, & Hofmann, 2019) mapped rotation and elastic strain field in the vicinity of an edge dislocation in tungsten by transferring the local HR-EBSD approach to off-axis TKD. They compared their measurements to numerical simulations convolved by the probe size. This echoes remarks regarding the application in SiGe/Si (Fig. 19), which will be further discussed in the next section.

Mapping elastic strains at the nanoscale in the SEM is pioneering work. As underlined in Chapter "Measuring elastic strains and orientation gradients by scanning electron microscopy: Conventional and emerging methods" by Ernould et al., accurate SEM calibration is an arduous task. Until present, publications focus on EBSD patterns, not TKD ones. Simulation of Kikuchi patterns acquired in transmission (Winkelmann et al., 2021) is nevertheless a first major step in this direction. Note that no mention is made regarding optical distortions or the way the projection geometry was determined in (Yu et al., 2019) or in (Tang et al., 2019), who first performed off-axis and on-axis HR-TKD using the local approach, respectively. To address the presence of diffraction spots, (Tang et al., 2019) placed 16 small subsets of 128×128-pixels aside from the pattern central region, while lattice rotations are limited to a few tenths of a degree. Regarding global HR-TKD approaches, applications have only been proposed by the present authors until now (Ernould, 2020; Dhinwal, Ernould, & Beausir, 2022; Ernould et al., 2020a, 2020b). The smoothness of elastic strains profiles in SiGe/Si (Fig. 19) as well as their qualitive agreements with the expected solution encourages further developments of the method at our lab. This implies the quantification of optical distortions of our cameras and use of more advanced calibration procedures, like the one by (Pang, Larsen, & Schuh, 2020), who shared their MATLAB code.

Applications to plastically deformed metals are difficult because of the presence of larger rotations and the degradation of diffraction contrast (Britton & Wilkinson, 2011; Maurice et al., 2012). Accurate elastic strain measurements in metallic materials is usually limited to slightly deformed samples. Regarding global HR-EBSD, (Shi et al., 2019) reported strain measurement uncertainty of 3.6×10^{-5} at the onset of plasticity in polycrystalline 316 L stainless steel. From this standpoint, the applications in quenched ODS steel, 15% deformed IF steel or nanostructured aluminum are challenging and original. Such microstructures are barely characterized by HR-EBSD/TKD since elastic strain measurement is compromised. As underlined by (Tanaka & Wilkinson, 2019), the accuracy of their calibration technique, degrades in the vicinity of an indent as compared to other regions of an IF steel specimen annealed at 700 °C for 1 h.

For all applications proposed using the Zeiss Supra 40 FEG-SEM and indexing by the Bruker ESPRIT 1.9 software, dislocation structures below ~2° disorientations are completely missed by standard HTI (Figs. 4B, 8B, and 15B). Analysis of the results in IF steel show that HTI succeeds in determining the disorientation angle, but it lacks accuracy regarding the disorientation axis (Fig. 11). Granted, no smoothing was applied to crystal orientations, but GND densities describe discontinuities of the crystal. With smoothing, the components of the Nye tensor would be strongly underestimated. Their estimation is already limited by the two-dimensional nature of EBSD/TKD maps. Moreover, the contribution of elastic strain is not assessable with indexing. This must be kept in mind when investigating slightly disoriented materials (<1°), this contribution being no longer negligible (Fig. 23C").

Despites the medium quality and resolution of the Kikuchi patterns, the proposed HR-EBSD/TKD approach succeeds in highlighting deformation structures, in particular fine details of the microstructures like isolated dislocations in ODS steel (Fig. 5). Beyond its angular resolution on the disorientation angle, its ability to determine the disorientation axis is essential. The gain as compared to indexing is of course particularly visible at low disorientation (<2°) but also at larger ones. More specifically, GND densities at subgrain boundaries involving disorientation up to 10–12° are quantified in the nanocrystalline aluminum sample (Fig. 15D). This is very uncommon as the HR-EBSD/TKD technique usually register patterns belonging to the same (sub)grain.

All results in deformed metals are here obtained at the expense of elastic strains, but their contribution to GND densities is negligible as compared to lattice curvatures (Jiang et al., 2015; Wilkinson & Randman, 2010). Moreover, knowledge of grain internal disorientations and GND densities is of paramount interest for understanding deformation mechanisms as well as for the development or validation of crystal plasticity models (Admal, Po, & Marian, 2018). Although questionable, it must be recognized that elastic strain mappings look nevertheless qualitatively relevant according to FSD imaging (Fig. 6 and in Fig. 16).

These results are promising given the SEM used lacks stability and its camera is not particularly tailored for HR-EBSD/TKD as compared to the one used for the application in GaN. The results in plastically deformed materials have therefore still a great margin of progress, just by improving the input data. In the previously cited work by (Shi et al., 2019), patterns with a resolution up to 4K and much higher signal-to-noise ratio are registered. Pattern filtering and weighting of the residuals in the IC-GN algorithm is another major area of improvement, which is detailed by (Shi et al., 2019, 2021).

5.2 Towards a fusion of calibration, indexing and HR-EBSD/TKD techniques?

Comparing global HR-EBSD/TKD measurements with lattice rotations derived from HTI may be disappointing in that new indexing methods (Chen et al., 2015; Foden, Collins, Wilkinson, & Britton, 2019; Hielscher, Bartel, & Britton, 2019; Lenthe, Singh, & Graef, 2019; Nolze, Hielscher, & Winkelmann, 2017; Nolze, Jürgens, Olbricht, & Winkelmann, 2018; Winkelmann, Jablon, Tong, Trager-Cowan, & Mingard, 2020; Winkelmann, Nolze, Cios, Tokarski, & Bała, 2020) determine orientations within up to 0.1–0.2° (Friedrich, Bochmann, Dinger, & Teichert, 2018; Lenthe et al., 2019; Ram, Wright, Singh, & Graef, 2017; Singh et al., 2018) for a well calibrated system (Ram et al., 2017). They are not used in this work since most of them were published in parallel and it should be remembered that the experimental part of this work was strongly impacted by the pandemic.

Overall, this chapter underlines that besides uncertainty in crystallographic orientations, the ability of indexing techniques to provide an accurate disorientation axis should be deeper investigated. Retrieving disorientations with 0.05° accuracy from indexing (Fig. 20C) is impressive. Unfortunately, it still results in noisy GND maps in GaN (Fig. 24A), because orientation gradients are also marginal. Note that indexed orientations are denoised with a tolerance angle of 0.1° to eliminate outliers. By smoothing and adjusting the scale, threading dislocations start appearing in Fig. 24B.

The latest release of AZtecCrystal-software employs the weighted burgers vector technique (Wheeler et al., 2009) to better evidence dislocation structures. Sensitivity on GND density is improved as compare to Fig. 24, based on the application in GaN single crystal available on the constructor's website (Oxford Instruments, n.d.), to which the reader is referred. The implementation of the weighted burgers vector technique is an improvement that can be transferred to HR-EBSD/TKD measurement as well.

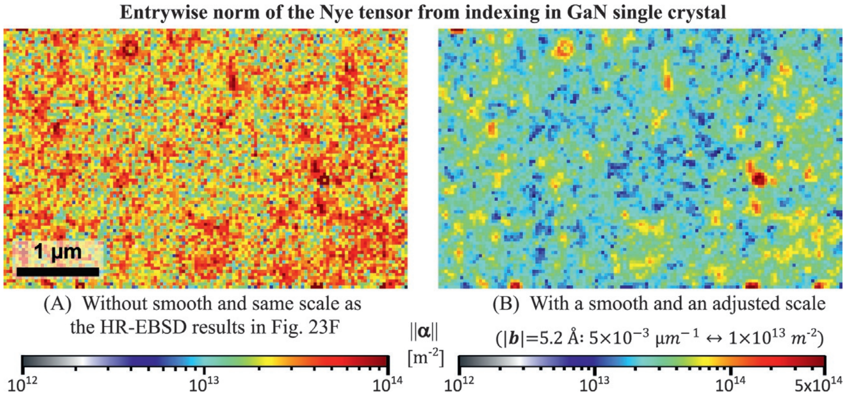

Fig. 24 Entrywise norm of the Nye tensor derived from indexing in GaN. (A) No smooth and same scale as the HR-EBSD measurements in Fig. 23F. (B) With a smooth and an adjusted scale.

Here, it should be kept in mind that the contribution of elastic strains is not negligible and that patterns in such a material (Fig. 20A) have overall a much better signal-to-noise ratio than most applications.

Actually, the question that should be raised is: to which extent can HR-EBSD/TKD complement indexing in plastically deformed materials? The HR-EBSD/TKD technique has been historically designed to characterize semiconductors. Rotations about a degree or more present in deformed metals rapidly appears as a limiting factor for measuring elastic strains. They have motivated the continuous development of the local approach since 2006 and the emergence of global ones more recently, as detailed in Chapters "Measuring elastic strains and orientation gradients by scanning electron microscopy: Conventional and emerging methods" and "Development of a homography-based global DIC approach for high-angular resolution in the SEM" by Ernould et al.. Deformed metals characterized in the present work constitute underexplored applications of the HR-EBSD/TKD technique. Yet, it arises in this chapter that the method can complement orientation mappings although elastic strains are questionable or simply ignored in the GND calculation.

Assuming HR-EBSD/TKD is offering a gain in accuracy for the characterization of plastically deformed materials, is the computational cost and data storage worth it? From this standpoint, distinction between indexing, calibration and HR-EBSD/TKD techniques is becoming unclear. For long, indexing was associated with low-resolution patterns, and HR-EBSD/TKD with high-resolution patterns leading to computationally expensive analyses.

Nowadays, the frontier between these two fields is vanishing. For instance, real-time indexing of high-resolution patterns (about 1000×1000 pixels) is performed by AZtec-software. On the contrary, dictionary and spherical harmonic indexing techniques rather consider low-resolution patterns with sometimes no visible Kikuchi bands, but their numerical cost is much higher than HTI. In some case, it is even comparable with HR-EBSD/TKD analyses. The datasets in ODS steel and IF steel consist of ~70,000 and ~80,000 patterns of size 600×600 pixels, respectively. Their analysis lasts 4h each when using a workstation with an Intel® Xeon® W-2145 processor (16 cores at 3.7 GHz). Using two Intel® Xeon® E5–2660 v3 processors with 20 cores each running at 2.6 GHz, dictionary indexing with refinement (Foden et al., 2019) requires 3.5 h to process ~9000 patterns of size 128×128 pixels.

Increasing synergies between all these techniques are expected in the future. They are more and more similar because of the algorithms they use, the comparison of experimental patterns with dynamical simulations or the need to take into account common phenomena such as optical distortions.

In terms of algorithms, simulation-based pattern matching is involved in recent progresses in indexing (Nolze et al., 2018), calibration (Friedrich et al., 2018; Winkelmann, Nolze, et al., 2020) and HR-EBSD/TKD (Kurniawan, Zhu, & DeGraef, 2021). The use of a reference simulated pattern has long been judged inadvisable for the HR-EBSD/TKD technique due to insufficient SEM calibration (Maurice et al., 2010). This is about to change. Global optimization is another common denominator of recent publications. Global image registration is at the heart of the revival of the HR-EBSD/TKD technique over the past few years (Ernould, 2020; Ernould et al., 2020a, 2021; Ruggles, Bomarito, Qiu, & Hochhalter, 2018; Shi et al., 2019; Vermeij, De Graef, & Hoefnagels, 2019; Vermeij & Hoefnagels, 2018; Zhu, Kaufmann, & Vecchio, 2020). It is also an trend observed regarding calibration techniques (Pang et al., 2020; Shi et al., 2021; Tanaka & Wilkinson, 2019; Winkelmann, Jablon, et al., 2020). Similarly to HR-EBSD/TKD, indexing and calibration need to account for optical distortions to become more and more accurate (Britton et al., 2010; Ernould et al., 2021; Maurice et al., 2011; Tanaka & Wilkinson, 2019; Winkelmann, Jablon, et al., 2020). More generally, the discussion in Chapter "Numerical validation and influence of optical distortions on accuracy" by Ernould et al. already pointed out that very similar DIC algorithms can be used to register diffraction patterns or to calibrate optical distortion models (Dufour, Hild, & Roux, 2014).

Without being exhaustive, it is quite clear that general trend is towards a fusion of techniques for pattern calibration, indexing and elastic strains assessment at once, provided that pattern quality allows it, which would be reminiscent of (Maurice & Fortunier, 2008).

5.3 On-axis HR-TKD: A compromise between SEM and TEM

In this chapter, the SEM used was pushed to the maximum of its capabilities when measuring elastic strains at the nanoscale in $Si_{0,69}Ge_{0,31}$ epitaxial layer (Fig. 19) or when characterizing deformation structures in a deformed nanostructure (Figs. 15 and 16).

For the first application, elastic strain profiles are qualitatively compared to NBED measurements in the TEM (Béché, 2009) (Fig. 19A,B). Quantitatively, ε_{xx} measured by on-axis HR-TKD (1.23%) is about twice lower than theory (2.10%). As already explained in Section 4.1.2, this is attributed to stress relaxation at the surface as well as the larger physical lateral resolution of the on-axis TKD technique. Further comparison with finite element analysis and probe size estimation by means of Monte Carlo simulations are required for a quantitative validation of the method.

Elastic strains profiles by on-axis HR-TKD are less noisy than those obtained by NBED, whose resolution is limited to 1×10^{-3} (Usuda et al., 2003) or 6×10^{-4} (Béché et al., 2009). (Cooper, Denneulin, Bernier, Béché, & Rouvière, 2016) compared different techniques for measuring elastic strains in the TEM. Beam precession in the nanobeam precession electron diffraction (NPED) technique (Rouviere et al., 2013) improves measurement accuracy to 2×10^{-4}. It is the most accurate technique along with dark field holography. Therefore, on-axis HR-TKD has a sensitivity to elastic strains like that achievable with TEM.

Regarding the characterization of deformed microstructures, the on-axis HR-TKD technique has several advantages over TEM, and few disadvantages.

First, FSD imaging is an asset for qualitative visualization of orientation gradients prior to orientation mapping. FSD contrast is indeed very sensitive to orientation change without the need to acquire images at different sample tilts, as in bright field imaging in the TEM. In addition, the use of three-color channels limits ambiguities as compared to grayscale images, where the same intensity can correspond to different orientations. The lateral spatial resolution of TEM is superior, with a probe size of up to 0.5 nm. Therefore, TEM imaging remains more suitable for visualizing dislocation networks, although FSD imaging can achieve this in some cases as shown in Fig. 25.

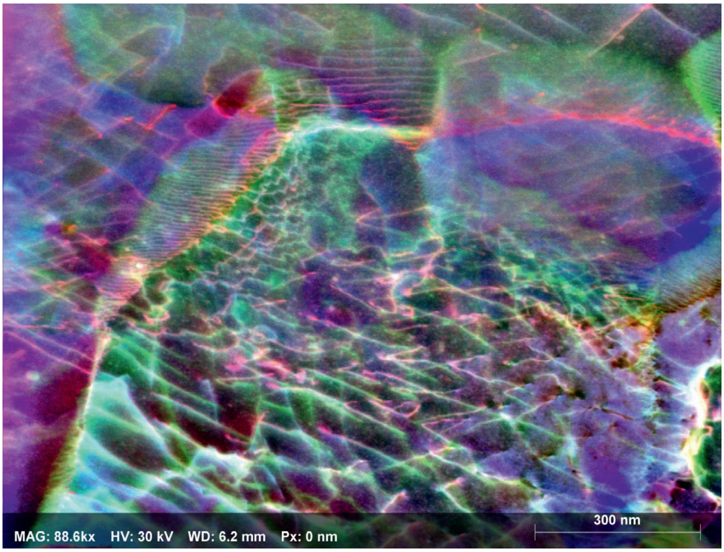

Fig. 25 FSD image of dislocation network in ODS steel.

The lower accelerating voltage of SEM leads to a wider beam broadening as it goes through the sample, but it also allows the TKD technique to be selective in depth. The superimposition of diffraction patterns is thus less likely than for TEM, whose non-selectivity in depth can make the pattern analysis cumbersome in nanocrystalline materials as there are several grains in the thickness. This difference was recently highlighted by (Mariano, Yau, McKeown, Kumar, & Kanan, 2020), who compared the ability of TKD and PED-ACOM (Precession Electron Diffraction - Automated Crystal Orientation Mapping) (Rauch & Veron, 2005) to map nanoparticles.

Finally, the application in nanocrystalline aluminum sample showed that high effective spatial resolution (3–10 nm) as well as high-angular resolution (0.01–0.03°) can be achieved simultaneously in a SEM using the on-axis HR-TKD technique (Fig. 16). Lattice rotations are measured from the displacement of Kikuchi bands, which is more sensitive to orientation changes than that of the diffraction spots considered by the PED-ACOM technique. The latter technique has an angular resolution on crystallographic orientations of the order of 0.8–1.1° (Morawiec, Bouzy, Paul, & Fundenberger, 2014; Viladot et al., 2013) and down to 0.3° using refinement algorithms matching experimental patterns to simulated ones (Rauch & Véron, 2014). As suggested by (Leff, Weinberger, & Taheri, 2015), the angular resolution of TEM could be improved by working with Kikuchi lines already used for the determination of crystallographic orientations (Fundenberger, Morawiec, Bouzy, & Lecomte, 2003; Zaefferer & Schwarzer, 1994).

In conclusion, the on-axis HR-TKD technique offers a compromise between TEM and SEM. While it is clear that a more expensive TEM is necessary for the most demanding applications in terms of lateral spatial resolution, the on-axis HR-TKD technique allows an equivalent resolution on elastic strains, as well as a superior angular resolution on rotations, to be achieved. Moreover, the depth selectivity of the method makes it a particularly suitable for the study of nanocrystalline materials, whose microstructure can be more easily visualized by FSD imaging prior orientation mapping.

6. Summary

- The proposed global HR-EBSD/TKD technique is applied to semiconductors and plastically deformed polycrystalline metals using EBSD and on-axis TKD techniques.
- Despite medium pattern quality and resolution, the sensitivity of the method allows fine details of the microstructure to be observed in plastically deformed metals. The relevance of the results is validated qualitatively by comparison with FSD imaging, whose contrast is very sensitive to orientation changes. Significant improvement over a standard analysis from on Hough-transform based indexing is achieved regarding the characterization of deformation structures, although accurate elastic strain measurement is compromised.
- For these materials, the contribution of elastic strains in the calculation of geometrically necessary dislocation densities appears negligible as compared to curvatures, which is in agreement with the literature (Jiang et al., 2015; Wilkinson & Randman, 2010). Conversely, elastic strains must be accounted for when disorientations are small ($\sim 0.2°$).
- In ideal experimental conditions like in the GaN single crystal, the method achieve a sensitivity better than 1×10^4 on elastic strain and rotation components, thus catching distortions caused by isolated threading dislocations. At 40 nm step size, this results in a sensitivity on GND densities of about 1×10^{13} m^{-2} (5×10^{-3} μm^{-1}).
- The on-axis HR-TKD technique allows an effective lateral spatial resolution of 3 to 10 nm and an angular resolution of 0.01 to 0.05° to be reached simultaneously in the SEM. The resolution on elastic strains

is comparable to the most accurate TEM methods (2×10^{-4}). Since Kikuchi bands are considered rather than diffraction spots, the sensitivity of on-axis HR-TKD on rotations is superior by on order of magnitude.

- The sensitivity of FSD contrast enable a fine observation of the microstructure before acquiring TKD orientation maps.

7. General discussion, perspectives, and conclusion

7.1 General discussion

This work is in line with several research axes of our lab. On the one hand, it proposes an original high-angular resolution approach for the characterization of microstructures in the scanning electron microscope. On the other hand, this method is coupled to EBSD, but also to an emerging experimental technique: on-axis TKD. This new configuration for the acquisition of electron diffraction patterns in transmission in the SEM was developed in our laboratory shortly before the beginning of the first author's thesis (Fundenberger et al., 2015, 2016). By coupling advanced experimental and data processing methods, this work aims to improve the observation and thus understanding of deformation mechanisms, particularly in polycrystalline materials.

In most crystalline materials, the occurrence of grain internal disorientations during plastic deformation is correlated with the formation of dislocation structures with a non-zero net Burgers vector, such as subgrain boundaries, dislocation cells or dislocation pile-ups. Their characterization requires the precise determination of the disorientation angle and axis as well as elastic strains, from which geometrically necessary dislocation densities can be calculated according to the Nye-Kröner theory (Kröner, 1958; Nye, 1953).

The literature review (Chapter "Measuring elastic strains and orientation gradients by scanning electron microscopy: Conventional and emerging methods" by Ernould et al.) and experimental results have highlighted the limitations of a standard processing of indexed crystal orientations when investigating deformation structures. Currently, real-time Hough-transform based indexing is the standard, but more accurate and noise robust techniques have been proposed in parallel of the present study. They are expected to replace HTI in the future as their speed increases and as they are implemented in user-friendly software. Beyond the uncertainty of crystallographic orientations, the applications proposed in this chapter clearly point out the necessity of determining the disorientation axis with accuracy.

The disorientation angle alone, even when it is known within 0.1°, is not sufficient to finely observed dislocation structures in terms of geometrically necessary dislocation densities for disorientations less than ~1°.

The so-called high-angular resolution techniques (HR-EBSD/TKD) have been specifically designed to measure relative crystal rotations as well as elastic strains, with an accuracy on the order of 1×10^{-4} (Villert et al., 2009; Wilkinson et al., 2006b). Although the local method has undergone many improvements since 2006, the presence of rotations larger than a few degrees remains its second largest source of error, after uncertainty in the projection geometry (Jäpel, 2014). The latter is propagated by the use of iterative remapping, and several questions are still surrounding the implementation of the method (section 4.1 in Chapter "Measuring elastic strains and orientation gradients by scanning electron microscopy: Conventional and emerging methods" by Ernould et al.). Therefore, this study progressively turned towards the development of an alternative method, potentially better suited to the characterization of plastically deformed polycrystalline materials, in which the LEM3 laboratory is particularly interested. The method remains nevertheless applicable to single crystals or semiconductors, as shown by the applications to SiGe/Si and GaN (Section 4), which are of particular interest for the electronics industry.

In Chapter "Development of a homography-based global DIC approach for high-angular resolution in the SEM" by Ernould et al., the literature review is extended to digital image correlation techniques for surface displacement and strain measurement. This has resulted in a novel global approach for HR-EBSD/TKD (Ernould et al., 2020a), which follows recommendations from literature.

Elastic strains and rotations are measured from a unique and large subset, avoiding questions or bias regarding number, size or position of small subsets used by the local approach. More importantly, the weighting of shift measurements when computing the solution is totally suppressed. The relative deformation of the subset is modeled by a linear homography, i.e., a plane geometry transformation involving eight parameters. It perfectly describes the displacement field on the scintillator between the reference and the target patterns, according to the mechanical model of the HR-EBSD /TKD technique. A homography not only accounts for the effects of lattice rotations and elastic strains at the scale at the scintillator scale, but also for the scale and translation induced by the displacement of the probe during scan (i.e., variations in projection geometry). The components of the deviatoric deformation gradient tensor are then deduced analytically from the measured homography, knowing the projection geometry and its variations.

The registration of the diffraction patterns by a numerically efficient inverse composition Gauss-Newton (IC-GN) algorithm is conducted independently of the projection geometry (section 2 in Chapter "Implementing the homography-based global HR-EBSD/TKD approach" by Ernould et al.). This differentiates the proposed method from the local HR-EBSD approach with remapping, but also from other global approaches published in parallel to this thesis, which considers the projection geometry during image registration (section 4.2 in Chapter "Measuring elastic strains and orientation gradients by scanning electron microscopy: Conventional and emerging methods" by Ernould et al.). The proposed method also integrates a correction of optical distortions in the IC-GN algorithm. Its principle is transferable to other global approaches based on a Gauss-Newton algorithm. Finally, the developed approach includes a global cross-correlation based initial guess to pre-align patterns disoriented up to about 10 degrees (sections 3 and 4.2 in Chapter "Implementing the homography-based global HR-EBSD/TKD approach" by Ernould et al.). It ensures the convergence of the IC-GN algorithm despite the presence of large rotations and/or elastic strains while being robust to the possible presence of discontinuities such as subgrain boundaries.

The method is programmed in FORTRAN and implemented in ATEX-software (Beausir & Fundenberger, 2017) developed at our laboratory. The accuracy and speed of uninterpreted code, as well as a graphical interface, make it quite easy to use. In addition to plotting and processing HR-EBSD/HR-TKD results, this software offers a complete environment for the analysis of EBSD/TKD data.

In Chapter "Numerical validation and influence of optical distortions on accuracy" by Ernould et al., the method is validated numerically from several thousand images obtained by deformation of a dynamically simulated pattern, in the absence and presence of first order radial distortion. The whole range of disorientation (0 to 14°) and equivalent elastic strain (0 to 5×10^{-2}) that the HR-EBSD/TKD technique can face has been investigated. This study quantifies the error committed when radial optical distortion is ignored. It demonstrates the need for a correction, contradicting the claim in the literature that neglecting the radial distortion induces a negligible error when the disorientation is small (<2°). Maximum errors greater than 1×10^{-4} (and 100% relative) are indeed observed on elastic strain components for distortion levels typical of EBSD cameras (fig. 9 in Chapter "Numerical validation and influence of optical distortions on accuracy" by Ernould et al.). More generally, it would be surprising if the HR-EBSD/TKD technique could dispense with a correction of optical distortions, while the errors induced by the latter are a major problem in the measurement of surface deformations in experimental mechanics (Pan, 2018; Pan, Yu, Wu, & Tang, 2013).

Several experimental applications of the method to EBSD and on-axis TKD patterns have been proposed considering materials with various thermomechanical states (Chapter "Applications of the method" by Ernould et al.).

Deformation structures have been characterized in plastically deformed metals, which constitute an underexplored field of application of the HR-EBSD/TKD technique. Plastically deformed metals are a very complex application, the plastic strain degrading diffraction contrast and thus worsening the calibration uncertainty. Yet, the method provides a real improvement due to its high sensitivity. It manages to accurately measure crystal rotations despite the medium quality of the diffraction patterns. Indeed, fine dislocation structures are revealed consistently with FSD imaging, whereas they are completely missed by standard analysis based on crystallographic orientations from HTI. Granted, elastic strain measurement in those materials is compromised, but their contribution to geometrically necessary dislocation densities appears negligible as compared to lattice curvatures (Fig. 9).

The study of deformed micro- or nanostructures is facilitated here by pre-realigning diffraction patterns using global cross-correlation techniques. This ensures a convergence of the IC-GN algorithm in the presence of grain internal disorientations up to 10–12°, no matter the presence of discontinuities such as subgrain boundaries. In particular, this is highlighted in nanocrystalline aluminum obtained by severe plastic deformation. Usually reserved for transmission electron microscopes, such a material is here investigated by means of on-axis HR-TKD. It simultaneously achieves high spatial resolution (3 to 10 nm) and a high angular resolution (0.01–0.03°) in a scanning electron microscope.

Finally, more standard applications have been considered, namely GaN single crystal and $Si_{0.69}Ge_{0.31}$ epitaxial layer. In the first case, a sensitivity of at least 1×10^{-4} is obtained on elastic strains and lattice rotations. The rotations being close to a tenth of a degree, the contribution of the elastic strains is no longer negligible in the calculation of GND densities, for which the noise floor is close to $5 \times 10^{-3}\ \mu m^{-1}$ ($1 \times 10^{13}\ m^{-2}$) at 40 nm step size. In the second case, elastic strain mappings are performed at the scale of a few nanometers by means of on-axis HR-TKD. Strain profiles are qualitatively in good agreement with the theory and nanobeam electron diffraction measurements in the TEM (Béché, 2009). Further developments are nevertheless necessary for quantitative elastic strain assessment. Stress relaxation caused by sample thinning must be accounted for as well as the physical spatial resolution of the technique. Despite technical limitations (uncertainty on the calibration and neglected optical distortion), the experimental results encourage further developments of the method.

7.2 Perspectives

Beyond the perspectives of improvement of the method discussed later, several practical limitations must be overcome. First, this work has highlighted the need to characterize optical distortion caused by camera lenses. Second, advanced calibration routines proposed recently must be implemented at our laboratory to reduce the uncertainty on projection geometry (Pang et al., 2020; Shi et al., 2021; Tanaka & Wilkinson, 2019; Winkelmann, Nolze, et al., 2020). It will then be possible to consider a quantitative validation of elastic strain measurement by the proposed method. A bending test is often considered to do so (Plancher et al., 2016; Shi et al., 2019; Villert et al., 2009). Theoretical elastic strain and rotation fields induced by a screw dislocation line near a free surface in GaN can also be simulated using dislocation models (Eshelby & Stroh, 1951) or piezoelectric dislocation frameworks (Han & Pan, 2012; Shi et al., 1999; Taupin et al., 2014) and compared to HR-EBSD measurements, in the spirit of (Yu et al., 2019) who used off-axis HR-TKD. The latter work can be transferred to on-axis TKD, for which study in SiGe/Si is in progress.

Attempts to characterize the optical distortions of our on-axis TKD camera have been initiated. The electron beam is focused on the scintillator while no sample present (Fig. 26A) and a "map" of several square millimeters is acquired at very low magnification (Fig. 26B). The position of the probe is easily identified by the white spot on the unfiltered images (Fig. 26B',B"). Aim is to obtain a grid of spots by superimposing all patterns. If there is no optical distortion, the spot spacing logically equals the map step size. This approach is inspired by (Mingard et al., 2011), who placed a thick block with a regular array of holes drilled through between the scintillator and a source light (Fig. 26C). Beam focusing on the scintillator is however inconclusive because the probe remains close to the scintillator's center as shown in Fig. 26D, where letters C_1 to C_4 denotes the corners of the "orientation map" in Fig. 26B.

Fortuitously, this study reveals that the scan direction differs by about 10° from that expected. Although scan rotation is off (0°), rows of the map do

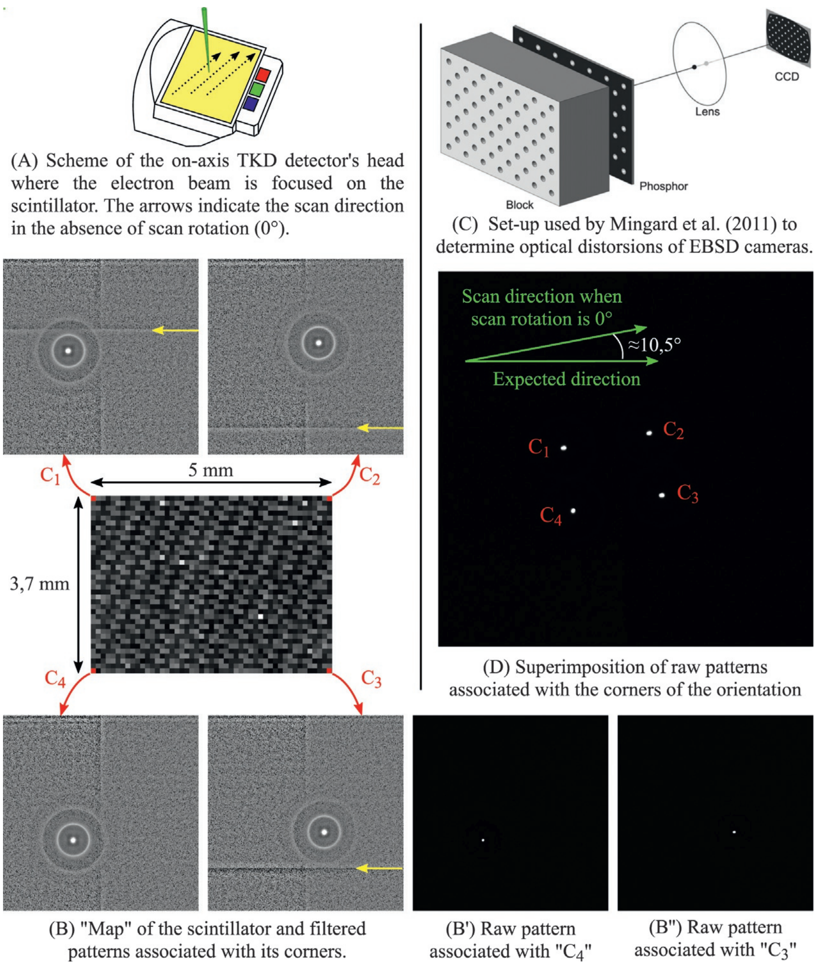

Fig. 26 (A) Scheme of the on-axis TKD detector on which the beam is focused. (B) Dimensions of the acquired "map" and filtered patterns associated with its corners marked by letters C_1–C_4. (B′, B″) Unfiltered images corresponding to the lower corners C_3 and C_4. (D) Superposition of unfiltered patterns associated with positions C_1–C_4. *Panel C: Image adapted from Mingard, K., Day, A., Maurice, C., & Quested, P. (2011). Towards high accuracy calibration of electron backscatter diffraction systems. Ultramicroscopy, 111(5), 320–329 showing the setup used for optical distortion determination.*

not correspond to a displacement of the probe parallel to the top edge of the scintillator. This angle must be taken into account when estimating the PC displacement within the orientation map. This experiment illustrates the need to verify the veracity of the information provided by the microscope and camera software.

Yellows arrows in Fig. 26B highlight readout artifact of the detector, which were recently pointed out by (Shi et al., 2021). They motivate further improvement of the method, especially in image filtering and residuals weighting during the IC-GN algorithm, as already discussed in section Chapter "Implementing the homography-based global HR-EBSD/TKD approach" by Ernould et al. Many code optimizations are still possible, starting with the parallelization of the IC-GN algorithm on GPU. The analysis times could be further reduced by optimizing the convergence definition of the IC-GN algorithm. The DIC analysis should be as free as possible from the bias linked to the user, who currently determines the filter parameters from a visual inspection of the images. In the work by (Shi et al., 2019), noise is reduced according to the residuals obtained after a first image registration.

Stochastic algorithms that are less sensitive to local optima than the IC-GN algorithm are likely to be developed as already mentioned in Chapter "Development of a homography-based global DIC approach for high-angular resolution in the SEM" by Ernould et al. As suggested by a recent work for pattern calibration (Tanaka & Wilkinson, 2019), genetic algorithm can be used for image registration as part of the HR-EBSD/TKD technique. Such kind of algorithm can also be used when computing the solution from the measured homography. The deviatoric deformation gradient tensor is currently deduced analytically for a given projection geometry. In the future, the projection geometry and its variations could be the degree of freedom of an optimization problem. They could vary within a range corresponding to their uncertainty so that the solution best satisfies the free surface condition of the sample ($\sigma_{i3} = 0$, in the sample frame).

The execution speed of the code, parallelized on CPU, is comparable to some emerging indexing methods. The proposed applications have been analyzed in a few hours, so that another use of the method could concern the determination of crystallographic orientations. Within a grain, pixels of the orientation map could be reindexed from the orientation of the reference (which would then be precisely determined beforehand) and the relative rotations of the crystal obtained by HR-EBSD/TKD. This is illustrated from the IF steel dataset in Fig. 27, which shows the inverse pole figure of [001]//Y according to standard indexing and after reindexing based on HR-EBSD measurements. This argues for the integration of calibration, indexing and high-angular resolution techniques into one, as discussed in Section 5.2.

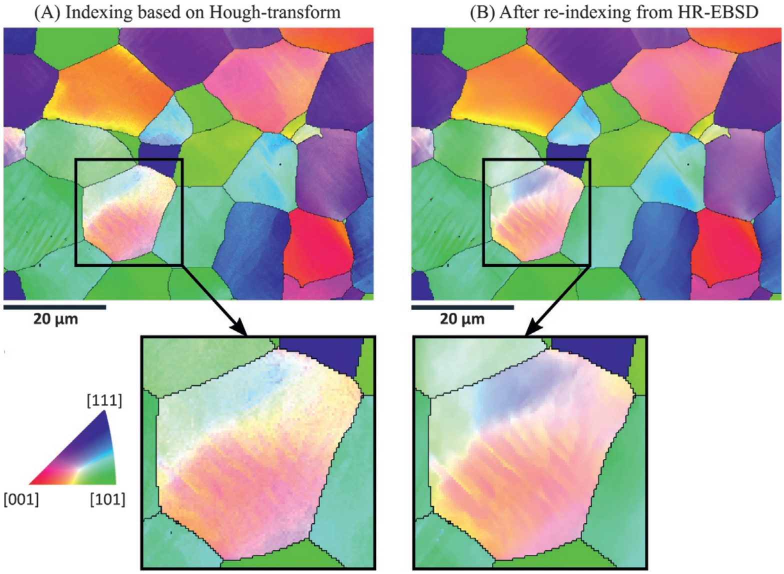

Fig. 27 Inverse pole figure ([001]//Y) of the IF steel dataset. (A) According to Hough-transform based indexing. (B) After reindexing according to the relative lattice rotations measured by HR-EBSD.

7.3 Conclusion

A global high-angular resolution method is proposed to measure relative lattice rotations and elastic strains within a crystal from Kikuchi patterns acquired in the SEM. It relies on global digital image correlation techniques to determine the displacement field between to patterns, from which the deviatoric deformation gradient tensor is deduced knowing the projection geometry and its variations.

Originality of the method is to model the displacement field in the scintillator by a linear homography. This line but not edge preserving geometric transformation perfectly accounts for the effects of elastic strains, rotations and probe displacement during scan. Its measurement is performed iteratively in the spatial domain by an inverse composition Gauss-Newton algorithm (IC-GN) from a unique and large region of interest. This algorithm is chosen since it is numerically efficient and widely used, and therefore benefits from constant improvements. The projection geometry is only considered after image registration, to analytically deduce the solution from the measured homography.

The IC-GN algorithm is modified to integrate a correction of optical distortions according to a model provided by the user and specific to the camera used. Such a correction is necessary for measuring elastic strains between 1×10^{-4} and 2×10^{-3}, especially at low disorientation angles (<1°). The extra computational cost of the correction is compensated by the absence of pattern pre-processing to correct distortion effects. The correction's principle is transferable to other global HR-EBSD techniques employing a Gauss-Newton algorithm.

The robustness of the method against disorientations up to about 10° and against discontinuities such as subgrain boundaries is ensured by a path-independent initial guess strategy. It pre-aligns patterns by means of Fourier-Mellin and Fourier-transform based cross-correlation algorithms, which estimate their relative in-plane rotation and translation, respectively. The method also adapts to the specificities of on-axis TKD images (diffraction spots and transmitted beam). Lattice rotations are estimated with an accuracy typically between 0.1 and 0.5°. It should be kept in mind that the method primarily aims at pre-aligning patterns and the effects of large elastic strains may be wrongly considered as rotations. Anyway, this method leads to convergence of the IC-GN algorithm in most of the experimentally or numerically investigated cases.

The homography-based global HR-EBSD/TKD approach is numerically validated in the presence of disorientations up to 14° or equivalent elastic strain up to 5×10^{-2}, i.e., over the range of values that the technique can be confronted with. This is performed considering optically undistorted patterns as well as patterns subject to various magnitude of first order radial distortion representative of EBSD cameras.

The method is applied to semiconductors and plastically deformed polycrystalline metals using both the EBSD and the on-axis TKD techniques. Despite the pattern medium quality, fine details of the microstructure in deformed metals are captured, as observed with FSD imaging. The contribution of elastic strains to geometrically necessary dislocation densities is negligible compared to that of the curvatures. Conversely, it must be accounted for when disorientations are small (~0.2°), like in GaN single crystal where the sensitivity on dislocation densities is close to 1×10^{13} m^{-2} (5×10^{-3} μm^{-1}) at 40 nm step size.

The on-axis HR-TKD technique allows an effective lateral spatial resolution of 3 to 10 nm and an angular resolution of 0.01 to 0.03° to be reached simultaneously in a scanning electron microscope. By being selective in depth, the technique is of particular interest for the study of nanocrystalline materials, in which patterns superimposition is more likely when using a TEM. Moreover, elastic strains are measured with a resolution comparable to the most accurate TEM methods (2×10^{-4}) in a $Si_{0.69}Ge_{0.31}$ epitaxial layer.

Finally, the method is programmed in FORTRAN in order to benefit from the computational speed of a non-interpreted language. It is implemented in the ATEX-software (Beausir & Fundenberger, 2017), which facilitates its future use.

References

Admal, N. C., Po, G., & Marian, J. (2018). A unified framework for polycrystal plasticity with grain boundary evolution. *International Journal of Plasticity*, *106*, 1–30. https://doi.org/10.1016/j.ijplas.2018.01.014.

Alkorta, J. (2013). Limits of simulation based high resolution EBSD. *Ultramicroscopy*, *131*, 33–38. https://doi.org/10.1016/j.ultramic.2013.03.020.

Beausir, B., & Fundenberger, J.-J. (2017). *Analysis tools for Electron and X-ray diffraction, ATEX - Software*. Université de Lorraine. www.atex-software.eu.

Béché, A. (2009). *Mesure de déformation à l'échelle nanométrique par microscopie électronique en transmission* (Thèse de doctorat, Institut National Polytechnique de Grenoble - INPG) https://tel.archives-ouvertes.fr/tel-00489867.

Béché, A., Rouvière, J. L., Clément, L., & Hartmann, J. M. (2009). Improved precision in strain measurement using nanobeam electron diffraction. *Applied Physics Letters*, *95*(12), 123114. https://doi.org/10.1063/1.3224886.

Brisset, F., Repoux, M., Ruste, J., Grillon, F., & Robaut, F. (2008). *Microscopie électronique à balayage et microanalyses*. EDP Sciences.

Britton, T. B., Maurice, C., Fortunier, R., Driver, J. H., Day, A. P., Meaden, G., et al. (2010). Factors affecting the accuracy of high resolution electron backscatter diffraction when using simulated patterns. *Ultramicroscopy*, *110*(12), 1443–1453. https://doi.org/10.1016/j.ultramic.2010.08.001.

Britton, T. B., & Wilkinson, A. J. (2011). Measurement of residual elastic strain and lattice rotations with high resolution electron backscatter diffraction. *Ultramicroscopy*, *111*(8), 1395–1404. https://doi.org/10.1016/j.ultramic.2011.05.007.

Brodu, E., & Bouzy, E. (2017). Depth resolution dependence on sample thickness and incident energy in on-Axis transmission Kikuchi diffraction in scanning Electron microscope (SEM). *Microscopy and Microanalysis*, *23*(6), 1096–1106. https://doi.org/10.1017/S1431927617012697.

Chen, Y.-H., Park, S. U., Wei, D., Newstadt, G., Jackson, M., Simmons, J. P., et al. (2015). *A dictionary approach to EBSD indexing. ArXiv:1502.07436 [physics, stat]* http://arxiv.org/abs/1502.07436.

Cooper, D., Denneulin, T., Bernier, N., Béché, A., & Rouvière, J.-L. (2016). Strain mapping of semiconductor specimens with nm-scale resolution in a transmission electron microscope. *Micron*, *80*, 145–165. https://doi.org/10.1016/j.micron.2015.09.001.

de Gironcoli, S., Giannozzi, P., & Baroni, S. (1991). Structure and thermodynamics of SixGe1-x alloys from ab initio Monte Carlo simulations. *Physical Review Letters*, *66*(16), 2116–2119. https://doi.org/10.1103/PhysRevLett.66.2116.

Dhinwal, S. S., Ernould, C., & Beausir, B. (2022). Facilitating the occurrence of dynamic recrystallization in plain extra low-carbon steel by warm asymmetric rolling. *Materials Characterization*, *189*, 111942. https://doi.org/10.1016/j.matchar.2022.111942.

Dufour, J.-E., Hild, F., & Roux, S. (2014). Integrated digital image correlation for the evaluation and correction of optical distortions. *Optics and Lasers in Engineering*, *56*, 121–133. https://doi.org/10.1016/j.optlaseng.2013.12.015.

El-Dasher, B. S., Adams, B. L., & Rollett, A. D. (2003). Viewpoint: Experimental recovery of geometrically necessary dislocation density in polycrystals. *Scripta Materialia*, *48*(2), 141–145. https://doi.org/10.1016/S1359-6462(02)00340-8.

Ernould, C. (2020). *Développement et application d'une méthode à haute résolution angulaire pour la mesure des gradients d'orientation et des déformations élastiques par microscopie électronique à balayage* (These de doctorat, Université de Lorraine) http://www.theses.fr/2020LORR0225.

Ernould, C., Beausir, B., Fundenberger, J.-J., Taupin, V., & Bouzy, E. (2020a). Global DIC approach guided by a cross-correlation based initial guess for HR-EBSD and on-axis HR-TKD. *Acta Materialia*, *191*, 131–148. https://doi.org/10.1016/j.actamat.2020.03.026.

Ernould, C., Beausir, B., Fundenberger, J.-J., Taupin, V., & Bouzy, E. (2020b). Characterization at high spatial and angular resolutions of deformed nanostructures by on-axis HR-TKD. *Scripta Materialia*, *185*, 30–35. https://doi.org/10.1016/j.scriptamat.2020.04.005.

Ernould, C., Beausir, B., Fundenberger, J.-J., Taupin, V., & Bouzy, E. (2021). Integrated correction of optical distortions for global HR-EBSD techniques. *Ultramicroscopy*, *221*, 113158. https://doi.org/10.1016/j.ultramic.2020.113158.

Eshelby, J. D., & Stroh, A. N. (1951). CXL. Dislocations in thin plates. *The London, Edinburgh, and Dublin Philosophical Magazine and Journal of Science*, *42*(335), 1401–1405. https://doi.org/10.1080/14786445108560958.

Estrin, Y., & Vinogradov, A. (2013). Extreme grain refinement by severe plastic deformation: A wealth of challenging science. *Acta Materialia*, *61*(3), 782–817. https://doi.org/10.1016/j.actamat.2012.10.038.

Foden, A., Collins, D. M., Wilkinson, A. J., & Britton, T. B. (2019). Indexing electron backscatter diffraction patterns with a refined template matching approach. *Ultramicroscopy*, *207*, 112845. https://doi.org/10.1016/j.ultramic.2019.112845.

Friedrich, T., Bochmann, A., Dinger, J., & Teichert, S. (2018). Application of the pattern matching approach for EBSD calibration and orientation mapping, utilising dynamical EBSP simulations. *Ultramicroscopy*, *184*, 44–51. https://doi.org/10.1016/j.ultramic.2017.10.006.

Fundenberger, J.-J., Bouzy, E., Goran, D., Guyon, J., Morawiec, A., & Yuan, H. (2015). Transmission Kikuchi diffraction (TKD) via a horizontally positioned detector. *Microscopy and Microanalysis*, *21*(S3), 1101–1102. https://doi.org/10.1017/S1431927615006297.

Fundenberger, J. J., Bouzy, E., Goran, D., Guyon, J., Yuan, H., & Morawiec, A. (2016). Orientation mapping by transmission-SEM with an on-axis detector. *Ultramicroscopy*, *161*, 17–22. https://doi.org/10.1016/j.ultramic.2015.11.002.

Fundenberger, J.-J., Morawiec, A., Bouzy, E., & Lecomte, J. S. (2003). Polycrystal orientation maps from TEM. *Ultramicroscopy*, *96*(2), 127–137. https://doi.org/10.1016/S0304-3991(02)00435-7.

Han, X., & Pan, E. (2012). Dislocation-induced fields in piezoelectric AlGaN/GaN bimaterial heterostructures. *Journal of Applied Physics*, *112*(10), 103501. https://doi.org/10.1063/1.4765722.

Hardin, T. J., Ruggles, T. J., Koch, D. P., Niezgoda, S. R., Fullwood, D. T, & Homer, E. R. (2015). Analysis of traction-free assumption in high-resolution EBSD measurements. *Journal of Microscopy*, *260*, 73–85. https://doi.org/10.1111/jmi.12268.

Hielscher, R., Bartel, F., & Britton, T. B. (2019). Gazing at crystal balls – Electron backscatter diffraction indexing and cross correlation on a sphere. *Microscopy and Microanalysis*, *25*(S2), 1954–1955. https://doi.org/10.1017/S143192761901050X.

Jäpel, T. (2014). *Feasibility study on local elastic strain measurements with an EBSD pattern cross correlation method in elastic-plastically deforming materials* (Rheinisch-Westfälischen Technischen Hochschule (RWTH) Aachen) http://publications.rwth-aachen.de/record/480096.

Jiang, J., Britton, T. B., & Wilkinson, A. J. (2015). The orientation and strain dependence of dislocation structure evolution in monotonically deformed polycrystalline copper. *International Journal of Plasticity*, *69*, 102–117. https://doi.org/10.1016/j.ijplas.2015.02.005.

Krieger Lassen, N. C. (1999). Source point calibration from an arbitrary electron backscattering pattern. *Journal of Microscopy*, *195*(3), 204–211. https://doi.org/10.1046/j.1365-2818.1999.00581.x.

Kröner, E. (1958). *Kontinuumstheorie der Versetzungen und Eigenspannungen*. Springer-Verlag. https://www.springer.com/de/book/9783540022619.

Kurniawan, C., Zhu, C., & DeGraef, M. (2021). Deformation state extraction from electron backscatter diffraction patterns via simulation-based pattern-matching. *Scripta Materialia*, *190*, 147–152. https://doi.org/10.1016/j.scriptamat.2020.09.004.

Leff, A. C., Weinberger, C. R., & Taheri, M. L. (2015). Estimation of dislocation density from precession electron diffraction data using the Nye tensor. *Ultramicroscopy*, *153*, 9–21. https://doi.org/10.1016/j.ultramic.2015.02.002.

Lenthe, W. C., Singh, S., & Graef, M. D. (2019). A spherical harmonic transform approach to the indexing of electron back-scattered diffraction patterns. *Ultramicroscopy*, *207*, 112841. https://doi.org/10.1016/j.ultramic.2019.112841.

Levinshtein, M. E., Rumyantsev, S. L., & Shur, M. S. (2001). *Properties of advanced semiconductor materials: GaN, AIN, InN, BN, SiC*. SiGe: John Wiley & Sons, Inc.

Mansour, H. (2016). *Caractérisation des défauts cristallins au MEB par canalisation d'électrons assistée par diagrammes pseudo-Kikuchi haute résolution: Application à l'acier IF, UO2 et TiAl* (Thèse de doctorat, Université de Lorraine) https://tel.archives-ouvertes.fr/tel-01611807.

Mariano, R. G., Yau, A., McKeown, J. T., Kumar, M., & Kanan, M. W. (2020). Comparing scanning Electron microscope and transmission Electron microscope grain mapping techniques applied to well-defined and highly irregular nanoparticles. *ACS Omega*, *5*(6), 2791–2799. https://doi.org/10.1021/acsomega.9b03505.

Maurice, C., Driver, J. H., & Fortunier, R. (2012). On solving the orientation gradient dependency of high angular resolution EBSD. *Ultramicroscopy*, *113*, 171–181. https://doi.org/10.1016/j.ultramic.2011.10.013.

Maurice, C., Dzieciol, K., & Fortunier, R. (2011). A method for accurate localisation of EBSD pattern centres. *Ultramicroscopy*, *111*(2), 140–148. https://doi.org/10.1016/j.ultramic.2010.10.007.

Maurice, C., & Fortunier, R. (2008). A 3D Hough transform for indexing EBSD and Kossel patterns. *Journal of Microscopy*, *230*(Pt 3), 520–529. https://doi.org/10.1111/j.1365-2818.2008.02045.x.

Maurice, C., Fortunier, R., Driver, J., Day, A., Mingard, K., & Meaden, G. (2010). Comments on the paper "Bragg's law diffraction simulations for electron backscatter diffraction analysis" by Josh Kacher, Colin Landon, Brent L. Adams & David Fullwood. *Ultramicroscopy*, *110*(7), 758–759. https://doi.org/10.1016/j.ultramic.2010.02.003.

Mingard, K., Day, A., Maurice, C., & Quested, P. (2011). Towards high accuracy calibration of electron backscatter diffraction systems. *Ultramicroscopy*, *111*(5), 320–329. https://doi.org/10.1016/j.ultramic.2011.01.012.

Morawiec, A., Bouzy, E., Paul, H., & Fundenberger, J. J. (2014). Orientation precision of TEM-based orientation mapping techniques. *Ultramicroscopy*, *136*, 107–118. https://doi.org/10.1016/j.ultramic.2013.08.008.

Niessen, F., Burrows, A., & Fanta, A. B.d. S. (2018). A systematic comparison of on-axis and off-axis transmission Kikuchi diffraction. *Ultramicroscopy*, *186*, 158–170. https://doi.org/10.1016/j.ultramic.2017.12.017.

Nolze, G., Hielscher, R., & Winkelmann, A. (2017). Electron backscatter diffraction beyond the mainstream. *Crystal Research and Technology*, *52*(1), 1600252. https://doi.org/10.1002/crat.201600252.

Nolze, G., Jürgens, M., Olbricht, J., & Winkelmann, A. (2018). Improving the precision of orientation measurements from technical materials via EBSD pattern matching. *Acta Materialia*, *159*, 408–415. https://doi.org/10.1016/j.actamat.2018.08.028.

Nye, J. F. (1953). Some geometrical relations in dislocated crystals. *Acta Metallurgica*, *1*(2), 153–162. https://doi.org/10.1016/0001-6160(53)90054-6.
Oxford Instruments. (n.d.). Dislocation Density Analysis of Crystals. Oxford Instruments. Retrieved April 14, 2022, from https://www.ebsd.com/ois-ebsd-system/dislocation-density-analysis.
Pan, B. (2018). Digital image correlation for surface deformation measurement: Historical developments, recent advances and future goals. *Measurement Science and Technology*, *29*(8), 082001. https://doi.org/10.1088/1361-6501/aac55b.
Pan, B., Yu, L., Wu, D., & Tang, L. (2013). Systematic errors in two-dimensional digital image correlation due to lens distortion. *Optics and Lasers in Engineering*, *51*(2), 140–147. https://doi.org/10.1016/j.optlaseng.2012.08.012.
Pang, E. L., Larsen, P. M., & Schuh, C. A. (2020). Global optimization for accurate determination of EBSD pattern centers. *Ultramicroscopy*, *209*, 112876. https://doi.org/10.1016/j.ultramic.2019.112876.
Pantleon, W. (2008). Resolving the geometrically necessary dislocation content by conventional electron backscattering diffraction. *Scripta Materialia*, *58*(11), 994–997. https://doi.org/10.1016/j.scriptamat.2008.01.050.
Pirouz, P. (1998). The origin of Nanopipes and micropipes in non-cubic GaN and SiC. *MRS Online Proceedings Library*, *512*(1), 113–118. https://doi.org/10.1557/PROC-512-113.
Plancher, E., Petit, J., Maurice, C., Favier, V., Saintoyant, L., Loisnard, D., et al. (2016). On the accuracy of elastic strain field measurements by Laue microdiffraction and high-resolution EBSD: A cross-validation experiment. *Experimental Mechanics*, *56*(3), 483–492. https://doi.org/10.1007/s11340-015-0114-1.
Polian, A., Grimsditch, M., & Grzegory, I. (1996). Elastic constants of gallium nitride. *Journal of Applied Physics*, *79*(6), 3343–3344. https://doi.org/10.1063/1.361236.
Ram, F., Wright, S., Singh, S., & Graef, M. D. (2017). Error analysis of the crystal orientations obtained by the dictionary approach to EBSD indexing. *Ultramicroscopy*, *181*, 17–26. https://doi.org/10.1016/j.ultramic.2017.04.016.
Rauch, E. F., & Veron, M. (2005). Coupled microstructural observations and local texture measurements with an automated crystallographic orientation mapping tool attached to a tem. *Materialwissenschaft und Werkstofftechnik*, *36*(10), 552–556. https://doi.org/10.1002/mawe.200500923.
Rauch, E. F., & Véron, M. (2014). Automated crystal orientation and phase mapping in TEM. *Materials Characterization*, *98*, 1–9. https://doi.org/10.1016/j.matchar.2014.08.010.
Rouviere, J.-L., Béché, A., Martin, Y., Denneulin, T., & Cooper, D. (2013). Improved strain precision with high spatial resolution using nanobeam precession electron diffraction. *Applied Physics Letters*, *103*(24), 241913. https://doi.org/10.1063/1.4829154.
Ruggles, T. J., Bomarito, G. F., Qiu, R. L., & Hochhalter, J. D. (2018). New levels of high angular resolution EBSD performance via inverse compositional gauss–Newton based digital image correlation. *Ultramicroscopy*, *195*, 85–92. https://doi.org/10.1016/j.ultramic.2018.08.020.
Shen, Y., Xu, J., Zhang, Y., Wang, Y., Zhang, J., Yu, B., et al. (2019). Spatial resolutions of on-Axis and off-Axis transmission Kikuchi diffraction methods. *Applied Sciences*, *9*(21), 4478. https://doi.org/10.3390/app9214478.
Shi, C., Asbeck, P. M., & Yu, E. T. (1999). Piezoelectric polarization associated with dislocations in wurtzite GaN. *Applied Physics Letters*, *74*(4), 573–575. https://doi.org/10.1063/1.123149.
Shi, Q., Loisnard, D., Dan, C., Zhang, F., Zhong, H., Li, H., et al. (2021). Calibration of crystal orientation and pattern center of EBSD using integrated digital image correlation. *Materials Characterization*, *178*, 111206. https://doi.org/10.1016/j.matchar.2021.111206.
Shi, Q., Roux, S., Latourte, F., & Hild, F. (2019). Estimation of elastic strain by integrated image correlation on electron diffraction patterns. *Ultramicroscopy*, *199*, 16–33. https://doi.org/10.1016/j.ultramic.2019.02.001.

Singh, S., Guo, Y., Winiarski, B., Burnett, T. L., Withers, P. J., & Graef, M. D. (2018). High resolution low kV EBSD of heavily deformed and nanocrystalline Aluminium by dictionary-based indexing. *Scientific Reports*, *8*(1), 1–8. https://doi.org/10.1038/s41598-018-29315-8.

Sun, S., Adams, B. L., & King, W. E. (2000). Observations of lattice curvature near the interface of a deformed aluminium bicrystal. *Philosophical Magazine A*, *80*(1), 9–25. https://doi.org/10.1080/01418610008212038.

Tanaka, T., & Wilkinson, A. J. (2019). Pattern matching analysis of electron backscatter diffraction patterns for pattern Centre, crystal orientation and absolute elastic strain determination – Accuracy and precision assessment. *Ultramicroscopy*, *202*, 87–99. https://doi.org/10.1016/j.ultramic.2019.04.006.

Tang, Y. T., Karamched, P., Liu, J., Haley, J. C., Reed, R. C., & Wilkinson, A. J. (2019). Grain boundary serration in nickel alloy inconel 600: Quantification and mechanisms. *Acta Materialia*, *181*, 352–366. https://doi.org/10.1016/j.actamat.2019.09.037.

Taupin, V., Fressengeas, C., Ventura, P., Lebyodkin, M., & Gornakov, V. (2014). A field theory of piezoelectric media containing dislocations. *Journal of Applied Physics*, *115*(14), 144902. https://doi.org/10.1063/1.4870931.

Troost, K. Z., Sluis, P.v.d., & Gravesteijn, D. J. (1993). Microscale elastic-strain determination by backscatter Kikuchi diffraction in the scanning electron microscope. *Applied Physics Letters*, *62*(10), 1110–1112. https://doi.org/10.1063/1.108758.

Usuda, N., Tezuka, S., Moriyama, N., & Takagi. (2003). Strain evaluation for thin strained-Si on SGOI and strained-Si on nothing (SSON) structures using nano-beam electron diffraction (NBD). In *2003 IEEE International Conference on SOI* (pp. 138–139). https://doi.org/10.1109/SOI.2003.1242928.

Vermeij, T., De Graef, M., & Hoefnagels, J. (2019). Demonstrating the potential of accurate absolute cross-grain stress and orientation correlation using electron backscatter diffraction. *Scripta Materialia*, *162*, 266–271. https://doi.org/10.1016/j.scriptamat.2018.11.030.

Vermeij, T., & Hoefnagels, J. P. M. (2018). A consistent full-field integrated DIC framework for HR-EBSD. *Ultramicroscopy*, *191*, 44–50. https://doi.org/10.1016/j.ultramic.2018.05.001.

Viladot, D., Véron, M., Gemmi, M., Peiró, F., Portillo, J., Estradé, S., et al. (2013). Orientation and phase mapping in the transmission electron microscope using precession-assisted diffraction spot recognition: State-of-the-art results. *Journal of Microscopy*, *252*(1), 23–34. https://doi.org/10.1111/jmi.12065.

Villert, S., Maurice, C., Wyon, C., & Fortunier, R. (2009). Accuracy assessment of elastic strain measurement by EBSD. *Journal of Microscopy*, *233*(2), 290–301. https://doi.org/10.1111/j.1365-2818.2009.03120.x.

Wheeler, J., Mariani, E., Piazolo, S., Prior, D. J., Trimby, P., & Drury, M. R. (2009). The weighted burgers vector: A new quantity for constraining dislocation densities and types using electron backscatter diffraction on 2D sections through crystalline materials. *Journal of Microscopy*, *233*(3), 482–494. https://doi.org/10.1111/j.1365-2818.2009.03136.x.

Wilkinson, A. J. (1996). Measurement of elastic strains and small lattice rotations using electron back scatter diffraction. *Ultramicroscopy*, *62*(4), 237–247. https://doi.org/10.1016/0304-3991(95)00152-2.

Wilkinson, A. J. (1997). Methods for determining elastic strains from electron backscatter diffraction and electron channelling patterns. *Materials Science and Technology*, *13*(1), 79–84. https://doi.org/10.1179/mst.1997.13.1.79.

Wilkinson, A. J., Meaden, G., & Dingley, D. J. (2006a). High resolution mapping of strains and rotations using electron backscatter diffraction. *Materials Science and Technology*, *22*(11), 1271–1278. https://doi.org/10.1179/174328406X130966.

Wilkinson, A. J., Meaden, G., & Dingley, D. J. (2006b). High-resolution elastic strain measurement from electron backscatter diffraction patterns: New levels of sensitivity. *Ultramicroscopy*, *106*(4), 307–313. https://doi.org/10.1016/j.ultramic.2005.10.001.

Wilkinson, A. J., & Randman, D. (2010). Determination of elastic strain fields and geometrically necessary dislocation distributions near nanoindents using electron back scatter diffraction. *Philosophical Magazine*, *90*(9), 1159–1177. https://doi.org/10.1080/14786430903304145.

Winkelmann, A., Jablon, B. M., Tong, V. S., Trager-Cowan, C., & Mingard, K. P. (2020). Improving EBSD precision by orientation refinement with full pattern matching. *Journal of Microscopy*, *277*(2), 79–92. https://doi.org/10.1111/jmi.12870.

Winkelmann, A., Nolze, G., Cios, G., Tokarski, T., & Bała, P. (2020). Refined calibration model for improving the orientation precision of Electron backscatter diffraction maps. *Materials*, *13*(12), 2816. https://doi.org/10.3390/ma13122816.

Winkelmann, A., Nolze, G., Cios, G., Tokarski, T., Bała, P., Hourahine, B., et al. (2021). Kikuchi pattern simulations of backscattered and transmitted electrons. *Journal of Microscopy*, *284*(2), 157–184. https://doi.org/10.1111/jmi.13051.

Yu, H., Liu, J., Karamched, P., Wilkinson, A. J., & Hofmann, F. (2019). Mapping the full lattice strain tensor of a single dislocation by high angular resolution transmission Kikuchi diffraction (HR-TKD). *Scripta Materialia*, *164*, 36–41. https://doi.org/10.1016/j.scriptamat.2018.12.039.

Zaefferer, S., & Schwarzer, R. A. (1994). Automated measurement of single grain orientations in the TEM. *Zeitschrifft Für Metallkunde*, *85*(8), 585–591.

Zhu, C., Kaufmann, K., & Vecchio, K. S. (2020). Novel remapping approach for HR-EBSD based on demons registration. *Ultramicroscopy*, *208*, 112851. https://doi.org/10.1016/j.ultramic.2019.112851.